

## ***Summary of professional accomplishments***

### **1. Personal data**

Name: **Ryszard Sobierajski**

Scientific degrees:

- Ph. D. degree in physics, *cum laude*: Warsaw University of Technology, Faculty of Technical Physics and Applied Mathematics, 10.10.2005, "Interaction of femtosecond pulses of the free electron laser with solids surfaces", prepared under supervision of prof. dr hab. Rajmund Bacewicz
- M.Sc. degree in physics, *cum laude*: Warsaw University of Technology, Faculty of Technical Physics and Applied Mathematics, 13.01.2000, "Studies of the damage threshold of metallic surfaces irradiated with ultrashort vacuum ultraviolet pulses", prepared under supervision of prof. dr hab. Rajmund Bacewicz

Employment in academic institutions:

- 2015 – present: assistant at the Laboratory of X-ray and Electron Microscopy Research, Institute of Physics Polish Academy of Sciences
- 2007 – 2010: Post-Doc position at the FOM Institute for Plasma Physics Rijnhuizen, Utrecht, Holland (currently FOM-Institute DIFFER Dutch Institute for Fundamental Energy Research) in the Advanced Applications of XUV Optics (AXO) nanolayer Surfaces and Interfaces department (nSI)
- 2005 – 2015: adjunct at the Laboratory of X-ray and Electron Microscopy Research, Institute of Physics Polish Academy of Sciences
- 1998 – 2002: guest scientist at HASYLAB, Deutsches Elektronen Synchrotron, Hamburg, Germany

### **2. Scientific achievement – major results**

As a main scientific achievement in the meaning of corresponding acts of law (Dz. U. 2016 r. poz. 882 ze zm. w Dz. U. z 2016 r. poz. 1311.) the series of five publications is presented with a common title:

#### ***„Mechanisms of structural modifications in selected solids with short-wavelength free electron lasers pulses”***

Series of publications forming the achievement (in the order of appearance):

[H1] A.R. Khorsand, **R. Sobierajski**, E. Louis, S. Bruijn, E.D. van Hattum, R.W.E. van de Kruijs, M. Jurek, D. Klinger, J.B. Pelka, L. Juha, T. Burian, J. Chalupsky, J. Cihelka, V. Hajkova, L. Vysin, U. Jastrow, N. Stojanovic, S. Toleikis, H. Wabnitz, K. Tiedtke, K. Sokolowski-Tinten, U. Shymanovich, J. Krzywinski, S. Hau Riege, R. London, A. Gleeson, E.M. Gullikson and F. Bijkerk, „*Single shot damage mechanism of Mo/Si multilayer optics under intense pulsed XUV exposure*”, Optics Express **18**, 700 (2010)

[H2] **R. Sobierajski**, S. Bruijn, A.R. Khorsand, E. Louis, R.W.E. van de Kruijs, T. Burian, J. Chalupsky, J. Cihelka, A. Gleeson, J. Grzonka, E.M. Gullikson, V. Hajkova, S. Hau Riege, L. Juha, M.

Jurek, D. Klinger, J. Krzywinski, R. London, J.B. Pelka, T. Plocinski, M. Rasinski, K. Tiedtke, S. Toleikis, L. Vysin, H. Wabnitz, F. Bijkerk, *Damage mechanisms of MoN/SiN multilayer optics for next-generation pulsed XUV light sources*”, Optics Express **19**, 193 (2011)

**[H3]** R.A. Loch, **R. Sobierajski**, E. Louis, J. Bosgra, F. Bijkerk, “*Modelling single shot damage thresholds of multilayer optics for high-intensity short-wavelength radiation sources*”, Optics Express **20**, 28200 (2012)

**[H4]** **R. Sobierajski**, M. Jurek, J. Chalupský, J. Krzywinski, T. Burian, S. D. Farahani, V. Hájková, M. Harmand, L. Juha, D. Klinger, R.A. Loch, C. Ozkan, J. Pelka, K. Sokolowski-Tinten, H. Sinn, S. Toleikis, K. Tiedtke, T. Tschentscher, H. Wabnitz and J. Gaudin, “*Experimental set-up and procedure for the investigation of XUV free-electron laser interaction with solids*” Journal of Instrumentation **8**, 2010 (2013)

**[H5]** **R. Sobierajski**, I. Jacyna, P. Dłużewski, M. T. Klepka, D. Klinger, J. B. Pełka, T. Burian, V. Hájková, L. Juha, K. Saksl, V. Vozda, I. Makhotkin, E. Louis, K. Tiedtke, S. Toleikis, R. Loch and J. Chalupsky “*The role of heat accumulation on the multi-shot damage of silicon irradiated with femtosecond XUV pulses at a 1 MHz repetition rate*” Optics Express **24**, 15468 (2016)

### 3. Detailed description of the achievement

#### 3.1. The scope of the work

My main scientific interest, after defense of PhD thesis, was devoted to the interaction of intense femtosecond pulses in the spectral range of extreme ultraviolet – XUV and X-ray with selected solids. In particular I have studied, both experimentally and theoretically, structural modifications of solids under irradiations with short-wavelength free electron lasers (FELs). I have developed specific experimental set-up and methods [H4]<sup>1</sup>. They were applied to investigate the radiation hardness of selected solids used in FEL optics - reflecting multilayer coatings for mirrors and bulk silicon, used as mirrors substrate or part of detectors. Achieved experimental results for Mo/Si [H1] and MoN/SiN multilayers [H2] allowed to formulate a theoretical model describing the physical process leading to structural modifications (damage) multilayer coatings. It was next applied to estimate the radiation hardness of FEL optics in the “water-window” spectral range [H3]. The studies of the interaction of solids with single pulses of femtosecond XUV radiation were further extended by investigation of the accumulation effects in case of multipulse irradiations of bulk silicon [H5]. My contribution to the above introduced work was crucial and it is presented here as my contribution to the understanding of mechanisms of structural modifications in selected solids with short-wavelength free electron lasers pulses, therefore is considered as the habilitation achievement. It is complemented by other publications related to the main topic of my studies, where I either was a one of the leading scientists or supported the performed research with experimental set-up and procedures developed by me.

#### 3.2. Introduction

The rapid development of short-wavelength free electron lasers operating in the XUV and X-ray regions has opened up unprecedented opportunities for generating high energy density states of matter. FELs [1-4] provide quasi-monochromatic and extremely intense pulses of radiation. Using FELs, it became possible to significantly extend the optical studies of structural phase transitions by systematic investigation of transition dynamics, energy transfer, accumulation of heat and damage. In case of the XUV and X-ray photons, the energy deposition process is not influenced by optical nonlinearities i.e. multiphoton absorption or free carrier absorption in non-metallic samples. Pulse length emitted by FELs is in the order of femtoseconds, much shorter than typical time constants related to structural transformations and to energy transfer processes. It is thus feasible to explore the dynamics of these processes separate from rapid radiation absorption. This dramatically simplifies modelling of physical processes leading to structural changes of matter.

Structural modifications can be induced by single or series (trains) of pulses with a repetition rate up to the megahertz range. In case of sources like FLASH, a superconducting FEL in Hamburg, the pulse spacing of 1  $\mu$ s is of the order of the typical time constant of heat dissipation from the solid sample surface to the bulk and is therefore suitable for studying heat accumulation processes.

Properties of the intense FEL beam create, apart new experimental opportunities, extreme demands to optics (mostly in terms of radiation hardness). FEL facilities rely on photon beamlines and experimental end-stations comprising several components (mirrors, grating monochromators, scintillators and radiation detectors) used to steer and shape the beam as well as to measure its position and properties – see e.g. [1]. For a proper design of optics for current and future short-wavelength FEL sources, it is crucial to understand the fundamental mechanisms leading to radiation damage - radiation induced structural modifications of optics.

In my work I have studied two extreme cases related to the topics of the radiation induced phase transitions in solids and radiation hardness of optics:

---

<sup>1</sup> References starting with “H” and “P” relate to the list of publications in Appendix 4

(1) multilayers used in FEL optics as mirror coatings, where the energy density absorbed from a single pulse was the highest and processes leading to structural modifications of the material occurred on very short scales – pico- and nanoseconds in time and nanometers in space [H1-H3],

(2) multipulse irradiations of bulk silicon (a typical material for optical substrates and detectors), where high energy densities were achieved due to the heat accumulation and processes relevant for radiation damage were much slower and occurred in the time scale of microseconds and on micrometer depths [H5]. Due to unprecedented properties of the radiation, the experimental work required development of a specific set-up and experimental procedures dedicated to studies of the interaction of XUV free electron laser (FEL) radiation with solids [H4].

**The main motivation for the presented studies was understanding of the fundamental structural modifications processes that occur in solids at intense photon loads as well as optics design for the new generation of XUV and X-ray light sources.**

### **3.3. Experimental set-up and procedures at FLASH [H4]**

#### **Introduction**

Properties of the intense FEL beam create extreme demands to experimental set-up and applied experimental methods. In compare to experiments in optical range I had to modify them to the applied significantly higher photon energy and to the rules of the access to the short-wavelength FEL – a synchrotron-like source. It was not possible to copy solutions used at synchrotrons due to much higher intensity and much shorter duration time of radiation pulses. Thus, I designed and optimized a specific set-up and experimental methods for systematic studies of radiation-induced structural changes in solids and applied in studies at the FLASH (Free electron LASer in Hamburg) facility, including experimental studies forming the achievement [H1, H2, H5] and other, related to it [P12, P14-P20, P22-P27, P29-P32, P37]. Below I describe the experimental beamline, sample positioning system and detectors. Further, I discuss experimental techniques like alignment, irradiation protocols, in-situ and ex-situ diagnostics and characterization of the main parameters of the interacting radiation. The set-up was presented in [H4] with examples of applications for FEL radiation tuned to 4.6 nm wavelength. However it was used in a broad spectral range within XUV regime – from 32 nm down 4.6 nm. In the presented summary I also discuss other examples from studies where I contributed as a co-author [H1, H2, H5, P12].

#### **FEL beam properties**

The experiments described within my habilitation work were performed at the FLASH facility [1]. The FEL beam was tuned to the wavelength centered at 13.5 nm (photon energy of 91.8 eV) with 0.1 nm bandwidth. The uncertainty about the absolute wavelength calibration was 0.1 nm while the bandwidth shot-to-shot fluctuation was found to be negligible. The pulse duration, evaluated from the FEL electron bunch charge, was tuned to either approximately 10 fs [H1,H2] or 100 fs [H5] (FWHM). The beam was linearly polarized and partly coherent [5]. Depending on the operating conditions (like pulse duration, repetition rate), the average energy per pulse was typically in the range of 1-100  $\mu$ J with peak values up to approximately 150  $\mu$ J. It was adjusted to the experimental needs with gas and/or solid attenuators with calibrated transmission. Since emission of the FLASH radiation is a stochastic process, the pulse energy fluctuated. For this reason the pulse energy downstream with respect to the gas attenuator was monitored by means of the gas monitor detector (GMD). The source could run at a maximum repetition rate of 10 Hz with up to 800 pulses in an 800  $\mu$ s-long bunch train. Single shot could be extracted by means of a beam shutter. The beam was steered to the experimental station along the BL2 or BL3 beamlines (see [1] for a detailed description). The beam was guided with grazing incidence flat mirrors coated with thin layers of a-C or Ni. It was focused with a 2 m focal length mirror (toroidal at BL2 and ellipsoidal at BL3 beamline).

The transmission of the beamline was estimated by calculating the reflectivity of each mirror. The maximal expected beamline transmission at 13.5 nm was 0.65. To obtain a Gaussian-like beam shape, circular apertures with various diameters (1, 3, 5 and 10 mm), placed up-stream to both the focusing mirror and the gas monitor detector, were used. Most of the experiments were performed in a “high intensity” mode, with samples placed at the focus position. The smallest focus spot diameter was of the order of 10  $\mu\text{m}$ , corresponding to a maximum achievable fluence of approximately 100 J/cm<sup>2</sup>. Measurements at lower intensities were performed using attenuators or with the sample placed away from the focus. At the furthest distance, e.g. for the purpose of sample’s adjustment, the FEL spot diameter was in the order of 2 mm and the corresponding beam’s fluence was well below any threshold for radiation damage.

### **Experimental set-up**

I developed a specific set-up and experimental methods for the systematic studies of radiation-induced structural changes in solids at the FLASH facility in Hamburg. The experiments were performed within a spherical ultra-high vacuum experimental chamber (see Figure 1). Similar set-up was developed during my PhD work and was described previously in reference [P8]. Since this publication several up-grades have been applied that were explained in detail in [H4]. The chamber was maintained under vacuum (typically 10<sup>-7</sup> mbar) by a turbo-pump (with minimum pressure in the order of 10<sup>-9</sup> mbar available with use of an ion pump). Samples of variable shape and dimensions (typically 10 x 10 mm<sup>2</sup>, up to few mm thick) were clamped on the sample holder I designed. Special mounting system was applied to minimize stress related sample’s deformation which might locally change the incidence angle of the FEL beam. The holder was a stainless steel plate mechanically polished in order to obtain flatness better than 20  $\mu\text{m}$  over 50 mm length, important for the minimization of the sample’s deformations, as well. In case of the experimental studies of the heat accumulation effects [H4] copper holder connected to an external heat sink was used to provide better heat conductivity and capacity of the holder and avoid the influence of the sample’s heating by the holder instead of radiation. The holder was attached using an electrically and thermally insulating coupling to a precision (1  $\mu\text{m}$  / 0.01° accuracy) motorized manipulator. It could be translated in Cartesian reference system (X, Y, Z) with 1  $\mu\text{m}$  precision and rotated around the vertical axis perpendicular to the beam direction with 0.01° accuracy in the 0-360° range. One of the axes of the manipulator (Z) was aligned parallel to the primary experimental axis defined by the centers of the entrance and exit flanges for the FEL beam. Moreover the center of the chamber lied approximately (within 1 mm distance) at the cross-point of the X-axis of the manipulator and the primary experimental axis.

The experimental chamber, including the motion stages and detectors, was mounted on an adjustable stand. It allowed precise alignment of the primary experimental axis with respect to the incident FEL beam. Since the FEL beam lied in the horizontal plane, in the most convenient set-up the YZ plane of the sample manipulator lied in the same plane, while the X-axis was vertical. Moreover, the stand allowed motorized translation of the chamber along the primary experimental axis with 0.1 mm accuracy. It was used to search for the best irradiation position (typically in the focus) and to change the spot size (hence varying the beam fluence at the sample surface).

I designed in-situ diagnostics consisting of the following elements: (a) XUV radiation detectors for reflected, scattered and transmitted photons: diodes, CCD cameras, multi-channel plate detectors, (b) time-of-flight (TOF) spectrometer of emitted charged particles [P8] and optical spectrometer for studying fluorescence and plasma emission [P37], (c) photocurrent detector, (d) video microscopes for sample monitoring and positioning with respect to the beam and for inspection of the irradiated spots, (e) pump-and-probe set-up for time-resolved microscopy studies [P12]. Most of detectors and all view ports were mounted on vacuum flanges (16 flanges enabling access to the chamber’s inside were available in total) and pointing to the interaction point at the center of the experimental chamber. Due to a modular

construction, the choice of the detectors could be adjusted to match the specific experimental requirements.

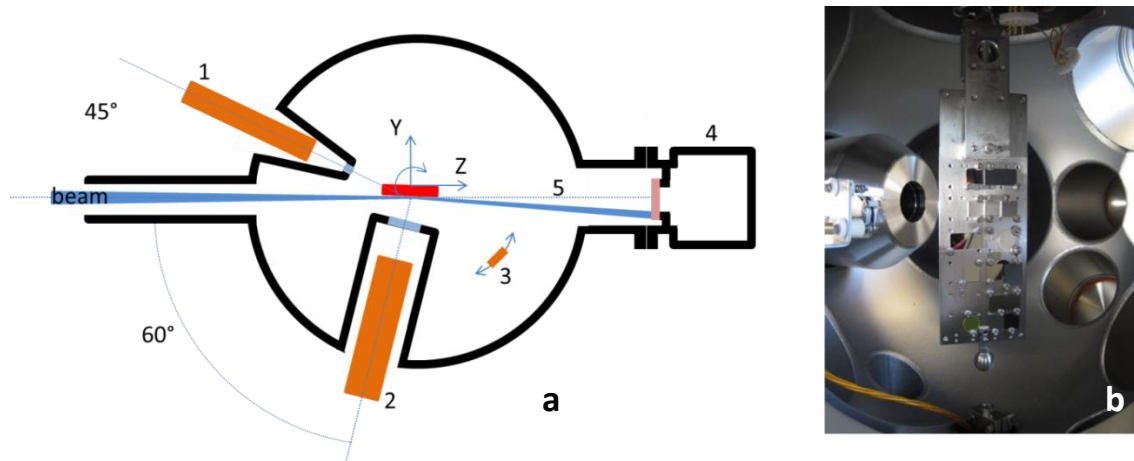


Figure 1 (a) Schematic view of the experimental chamber: 1 - online microscope for normal incidence irradiation, 2- high resolution online microscope for grazing angle irradiation, 3- MCP and photodiode, 4 - CCD camera, 5 - primary axis of the experimental chamber. (b) Picture showing the interior of the chamber with the sample holder, the inside flange of microscope (1) and the MCP (3). Figure adapted from [H4].

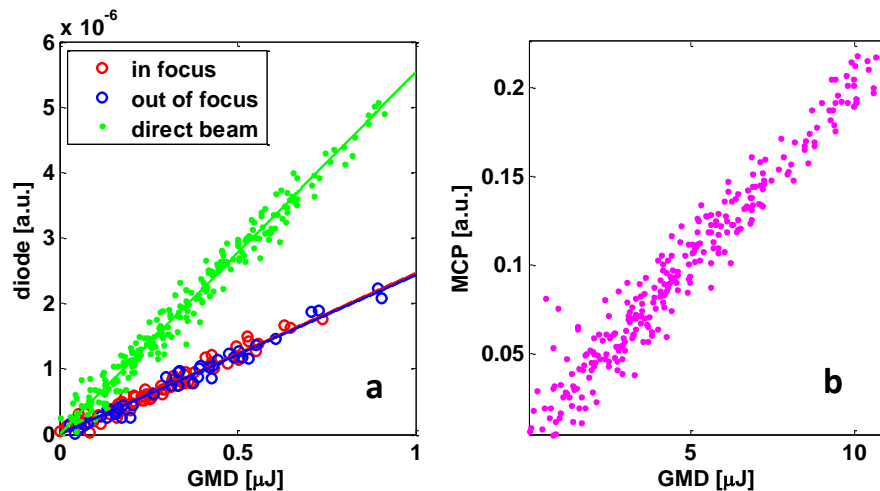


Figure 2 Correlation of the pulse energy measured by the GMD with the diode (a) and MCP (b). Colors on the figure (a) correspond to different sample and diode configuration: green – dataset for the diode placed directly in the incidence beam, blue and red – diode measures the reflected beam when the sample was out-of and in-focus, respectively. Solid lines correspond to the linear fits to the data. In- and out-of-focus data overlap since there was no reflectivity change between high and low intensity measurements (see H1 for details).

I developed a set of XUV radiation detectors for measuring of intensity of reflected, scattered and transmitted photons. An XUV CCD camera was used to monitor the position of the direct and reflected beam. It was mounted at the beam's exit flange at the back side of the experimental chamber. To avoid saturation, thin metallic foils in front of the detectors were used for attenuation (e.g. 50 nm Al, 3  $\mu\text{m}$  Si, 100 nm a-C). The reflected radiation intensity was measured with a photodiode. In case of the XUV reflectometry measurements of multilayer coatings [H1, H2], to avoid diode saturation, it was coated with

350 nm molybdenum and 500 nm silicon layers and in addition it was preceded by a 0.28  $\mu\text{m}$  thick aluminum foil attenuator. The coating on the diode's surfaces diminished the contamination of the signal by optical radiation. A Chevron-type Microchannel Plate (MCP) detector was used to measure the intensity of the scattered light. The effective area of the MCP detector was of the order of 1  $\text{cm}^2$ , no apertures were placed in front. The electrical signals were measured by a 1 GHz oscilloscope without any amplification. The MCP bias voltage was adjusted in the range of 1000-2000 V to optimize the amplitude of the signal at the oscilloscope. Both detectors were mounted on a rotational arm inside the experimental chamber at approximately 140 mm distance from the sample (see Figure 1). The rotation of the detectors was coaxial with the sample's rotation allowing for angular resolved measurements. In particular, in case of the reflectivity measurements, it enabled to determine the absolute reflectance (see Figure 2). For that purpose I proposed the following procedure. First the filter/diode combination was characterized using the direct beam – the slope of the line fitted to the correlation plot of photodiode and GMD signals was calculated. Next the diode measured the intensity of the radiation reflected from the sample and a slope of a line fitted to the correlation plot was obtained. The absolute reflectivity of the sample was calculated as a ratio of both slope parameters – for reflected and direct beam, respectively. I tested the detectors with use of the unfocused beam by measuring the amplitude of the MCP and photodiode signal as a function of the pulse energy obtained by the GMD. The photodiode signal correlated very well with the incidence photon energies, while MCP and GMD signals correlated only roughly (see example at Figure 2(a) and (b) for photodiode and MCP, respectively). The limited correlation was most probably caused by the pointing instability of the FLASH beam which results in irradiation of slightly different places from shot to shot, and changes of the intensity and angular distribution of the scattered light.

Measurements of the intensity of the reflected and scattered radiation could provide information about the sample's optical degradation during multishot exposures. For similar reason I proposed to measure the photocurrent during irradiations. The ionizing FEL radiation led to the emission of electrons from the samples, which process is very sensitive to the surface structure.

Apart from the detectors used for radiation and photocurrent measurements, two long range microscopes (devices 1 and 2 in Figure 1) were attached to the experimental chamber. They were used to monitor the surface of the sample and to position the sample with respect to the beam. Since the beam diameter on the sample in the focus was of the order of 10  $\mu\text{m}$ , high resolution ( $\sim 1\text{-}2 \mu\text{m}$ ) microscopic imaging was necessary. Inlet flanges were used to minimize the working distance.

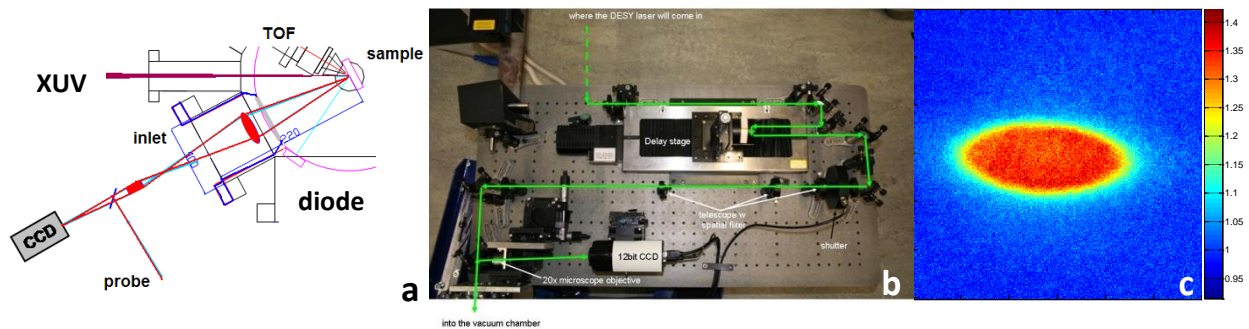


Figure 3 (a) Schematic layout of the XUV pump - optical probe set-up. XUV beam irradiated the sample in the center of the UHV experimental chamber. The laser probe beam illuminated the irradiated spot at normal incidence and after reflection was recorded with a CCD camera. To provide the required spatial resolution of the imaging system relay optics inside inlet and the camera objective were used. (b) The arrival time of the laser probe beam with respect to the XUV beam was controlled by a delay stage. (c) Time resolved microscopy image of the spot at the Mo/Si multilayer optical coating irradiated with FLASH pulse at 10 ps delay time. Colors correspond to sample reflectivity relatively to the unirradiated area (see colorbar at the side of the figure).

I proposed to use the time resolved microscopy in the XUV pump – optical probe mode to study the dynamics of the structural changes of the irradiated multilayers [H1]. The XUV pulse excited the surface

of the sample. A time-delayed optical probe pulse of 800 nm wavelength and 100 fs duration, synchronized to the FEL with accuracy better than 2 ps, served as illumination for an optical microscope. The optical delay line and microscope itself were mounted on the air side on an optical breadboard attached to the vacuum chamber's stand (see Figure 3(a) and (b)). Due to the geometrical constraints related to the sample's holder movement and TOF spectrometer mounted inside the experimental chamber, the proximity to a viewed object was not feasible. Thus the relay optics inside the inlet flange was used. Vacuum window with optical coatings were used to reduce the reflections and light scattering on optics. The pump-probe setup allowed to measure the evolution of the optical pulse reflectivity of the XUV irradiated surfaces with temporal and spatial resolution. An example of the time resolved microscopy image of the spot at the Mo/Si multilayer optical coating irradiated with FLASH pulse [H1] at the first stage of the structural modifications – melting - at 10 ps delay time is presented on Figure 3(c).

### Alignment procedures

In contrary to the most of experimental stations at synchrotron facilities, the presented set-up at FLASH facility was not attached permanently to the beamline. Furthermore the applied detectors were modified from one beamtime to another. Thus precise alignment procedures were developed with my attendance and performed under my supervision before each experiment. They were optimized with respect to the required time due to the limited available beamtime. The procedures were done in the following order: (1) alignment of the chamber position and axis, (2) determination of the sample coordinates, (3) determination of the focus location, (4) absolute calibration of the incidence angle.

First, the stand was roughly aligned such that the center of the chamber was approximately at the FEL beam position. The pre-alignment was done using a He-Ne laser beam which is collinear with the FEL beam. The position of the interaction point on the sample holder, the orientation of the primary experimental axis w/r to the incidence beam and the angular orientation of the sample holder were adjusted. Similar alignment procedures were repeated using the FEL beam and plasma emission from metals or fluorescence from a Ce:YAG crystal.

Next, samples were installed on the sample holder, usually in clean room conditions. The sample holder was mounted on the manipulator, with angular and height accuracy better than  $0.1^\circ$  and  $100\ \mu\text{m}$ , respectively. A coordinate system was defined for each sample, with the horizontal and vertical axis, lying in the plane of the sample surface. The system was used to map the translation of the FEL beam with respect to the sample surface.

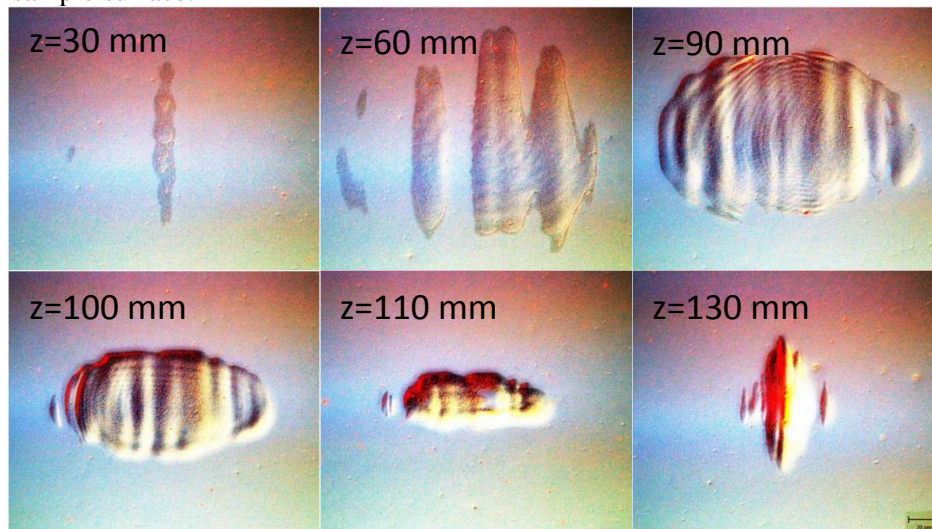


Figure 4 FEL beam imprints on PMMA made at different positions of the experimental chamber (Z scan) as observed ex-situ by means of DIC microscopy. The chosen best focus position during the experiment was  $Z=90\ \text{mm}$ .

An important step of the alignment procedure was to find the position of the samples with respect to the focus. It was based on the analysis of the FEL beam imprints on a selected target (usually poly(methyl methacrylate) - PMMA) made at different positions of the experimental chamber and observed in-situ by means of the video microscope (see Figure 1(a)). Due to the astigmatism of the X-ray focusing optics one observed the change in the shape of the imprints while scanning through the focus (as shown in the ex-situ measurements in Figure 4). The position where imprints showed the roundest shape, e.g. corresponding to the position  $Z = 90$  mm in Figure 4, was chosen for most of the measurements. The ex-situ analysis confirmed the accuracy of this method. Next, the optimal position of the sample's surface with respect to the focus was adjusted taking into account the respective thickness of each sample. For that purpose I proposed to measure the samples thickness using the depth of focus of the optical microscopes what provides better than  $50 \mu\text{m}$  accuracy.

The last step was to precisely define the angular orientation of the samples enabling control of the incidence angle. In case of bulk samples irradiated at normal incidence or multilayers at incidence angle close to normal, it was assumed that both normal to the sample surface and to the sample holder were collinear [H1,H2,H5]. However, in the case of single layer optical coatings irradiated at grazing incidence angles [P17, P24, P26], a more accurate procedure was necessary to obtain the required angular precision better than  $0.3^\circ$ . For that purpose I proposed the following procedure. Two images were taken with a XUV CCD camera placed at the exit flange of the experimental set-up. The position of the beam reflected from a sample at grazing incidence was compared to the position of the direct beam (see Figure 5). The grazing angle  $\theta$  could be deduced from the simple geometrical analysis. For this procedure, the flatness of the samples was crucial. It appeared that in almost all cases it was better than  $0.1^\circ$ .

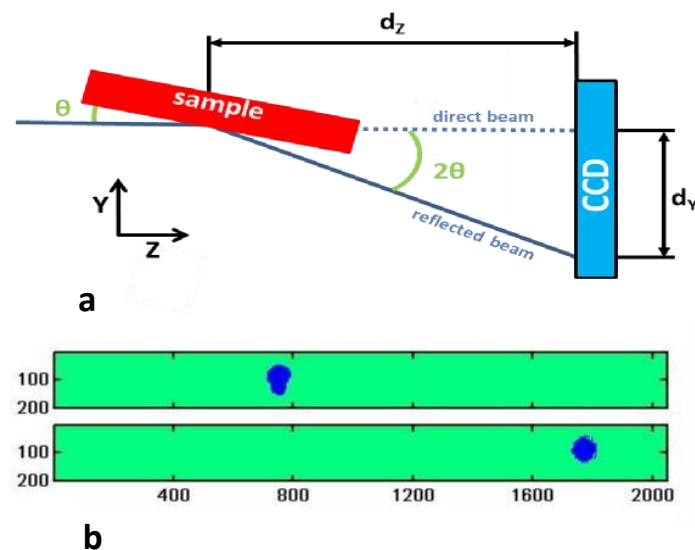


Figure 5 (a) Schematic layout of the grazing incidence calibration method. (b) Processed images from the CCD camera for the direct (upper image) and reflected (lower image) beams. The colors correspond to the pixels above (blue) and below (green) threshold of 44 000 counts. The axis labels correspond to CCD camera pixels. Pixel saturation and crosstalk can be observed on the direct beam image. Figure adapted from [H4].

### Irradiation procedures and characterization techniques

I developed the following irradiation procedures and proposed necessary characterization techniques. In most cases samples were irradiated in single shot mode, i.e., after each irradiation the sample was moved to a new position. For each shot the pulse energy, sample number, the position of the irradiation spot in the sample's coordinate system and signals from the detectors were registered. Since only a rough

estimate of the damage threshold was available prior to the irradiation, the pulse energy was varied over two orders of magnitude. This was achieved in two ways – by using the wide distribution of pulse energies around the mean value (due to the stochastic properties of the FEL radiation) and adjusting the average pulse energy by means of gas and solid attenuators. When the stochastic fluctuations of the FEL radiation were weak, the level of the (gas) attenuation was changed continuously, providing smooth variations of the pulse energy over a desired range. The online microscopes allowed monitoring the appearance of damage (if it was strong enough like ablation), and adapting the pulse energy. The irradiated samples were then examined already during the beamtime using optical microscopy with differential interference contrast - DIC (with Nomarski prism) to confirm that the pulse fluence range (defined by their energy and beam size on the sample) went beyond the damage threshold level for each sample. As induced structural modifications could be extremely faint and difficult to find, the defined irradiation matrix and irradiation markers were necessary for their characterization.

In multishot irradiation mode, the samples were exposed to many FEL pulses at the same position. In general irradiation procedures were similar to the ones of the single shot exposures. It was important to reduce the pulse fluence well below the surface modification's threshold energy for single shot exposures and to minimize the energy fluctuations. Otherwise, due to stochastic nature of the radiation, a single pulse with high energy could exceed this limit and the final structural changes of the sample would result from a mixture of irradiation conditions (single and multishot). Another important requirement was that of beam stability. Two apertures at a large distance were used to define the optimal direction of the beam resulting in minimization of the spot position variations on the sample. The irradiated spots were investigated after the beam time with similar techniques as in the case of single shot exposures.

Structural and morphological changes induced in the various materials under single and multi-shot irradiations had to be correlated with the incident radiation's parameters. While many of them (like wavelength, pulse energy) were provided by the FEL facility, the focused beam profile had to be characterized. The material's response to FEL radiation may depend non-trivially on the local fluence and/or irradiance, therefore, an incorrect assumption on the beam profile could lead to inaccurate interpretation of the data. Usually, the FEL beams cannot be treated in a Gaussian approach. During the first experiments [**H1,H2**] the irradiated spot consisted of a few semi-gaussian parts. The beam size (characterized by, so called, effective area) of each part and corresponding portion of the pulse energies were unknown. I developed a procedure to calculate both parameters for each part of the beam. It was based on the observation of the threshold behavior of the structural modifications under irradiations with XUV beam and the assumption that damage threshold does not depend on the incident beam intensity and size. The procedure allowed to establish the main beam parameters and to calculate the damage thresholds for Mo/Si and MoN/SiN multilayers irradiated at FLASH [**H1, H2**].

In many other experiments the beam profile was even more complex and the above mentioned procedure could not be applied. In order to characterize the focused beam a method based on single-shot ablation imprints in PMMA (for 13.5 nm radiation) was used [**H4, P23**]. This method assumed that the PMMA ablation threshold  $F_{th}$  remained constant and independent of the impinging peak fluence  $F_0$  and any energy transport processes like diffusion. Consequently, the ablation (surface) contour corresponded to the beam contour at the fluence level  $F_{th}$ . This contour could be measured, for example, by means of DIC microscopy with Nomarski prisms. By creating, so called, fluence scan – a data set correlating the area within the ablation contour with incidence pulse energy – one could obtain the effective area of the irradiating beam. This parameter could be further used to calculate the damage threshold of other samples. Moreover, the PMMA imprints allowed to directly map the distribution of the radiation fluence over the spot. It was based on the AFM map of the surface height/depth over the spot together with the effective area and irradiating pulse energy. Apart from the above mentioned assumptions, it required an exponential in-depth profile of the absorbed radiation followed by exponential dependence of the crater depth on the local beam fluence. During research in which I participated it was shown, that these conditions were fulfilled over a wide range of radiation wavelength, incident angle and photon pulse duration.

The effects of irradiation – induced structural changes - were characterized using different analysis techniques. One of the great challenges of these analyses was to perform measurements on micron sized structures - the typical diameter of the damaged areas. Two main measurements types were performed: surface analyses providing information on the shape/morphology of the irradiated spots, and structural analyses.

Morphological analyses included: optical DIC microscopy with Nomarski prism sensitive to changes of the morphology and optical properties of the materials, white light interferometry (WLI), atomic force microscopy (AFM) providing a 2D depth map and scanning electron microscopy (SEM) showing the morphology of irradiated spots (see examples on Figure 6). The optical DIC microscopy with Nomarski prism measurements, which were fast and easy, could be performed on all irradiated spots (typically a few hundred – few thousands of places at various samples during one beamtime ) and were used to determine the damage threshold. From this global survey few representative spots were selected to perform more demanding analyses, like AFM, WLI, SEM or TEM.

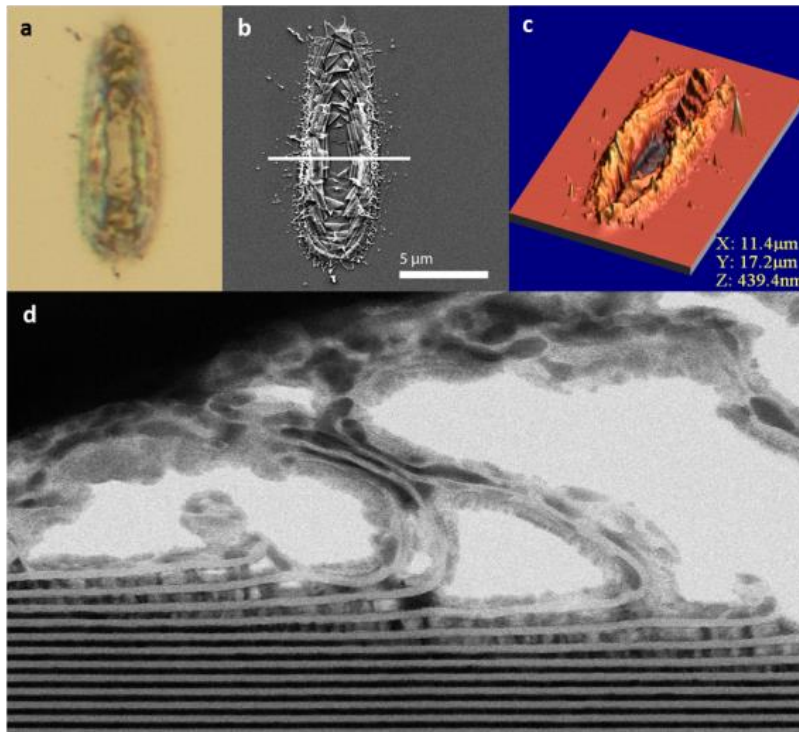


Figure 6 Damage to MoN/SiN multilayer induced by 13.5 nm FLASH beam: (a) optical DIC microscopy, (b) scanning electron microscopy with a with line in the center of the irradiation spot marking position of the cross-section cut, (c) atomic force microscopy, (d) transmission electron microscopy image of part of the cross-section marked on (b).

The second type of analysis provided information on the electronic properties, local and long range atomic order modifications induced by radiations. Electronic properties were investigated by scanning photoelectron microscopy (SPEM) using synchrotron radiation [P27]. Local atomic order was investigated by micro-Raman spectroscopy [P27], a microbeam scattering technique. X-ray diffraction was performed to characterize the formation of strain in the vicinity of the irradiated spots [P25, P28, P33]. One of the most informative and important techniques was Scanning transmission electron microscopy (STEM) applied to analyze the structural changes below the irradiated surface [H1, H2, H5]. This method, which implied to “cut” a slice (cross-section) of irradiated spot using focused ion beam (FIB), destroyed the sample and had to be performed after all other measurements.

### 3.4. Radiation hardness of Mo/Si multilayer coatings for FEL optics [H1]

#### Introduction

Multilayer coated optics is nowadays a standard for control of XUV and X-ray radiation in many fields of science and technology [6-8]. It can fulfill the extreme requirements in terms of figure errors and roughness, wavefront preservation, and stability in the XUV and soft X-ray regime. It has experienced a considerable technology boost due to the application in advanced photolithography. As a result, very stable, high reflectance coatings were developed [9].

At FLASH source, multilayer coated optics were used in “front-line” experiments like XUV time resolved holography as a part of the imaging system [10] and as diffraction limited XUV beam focusing optics for warm dense matter (WDM) creation [11]. The radiation intensity at FEL sources is very high and e.g. for 13.5 nm wavelength can reach even  $10^{10}$  W/cm<sup>2</sup> at the optical elements like off-axis parabola used in WDM experiments. This is at least 6 orders of magnitude higher than in a typical lithography application. Potential damage of the optics has to be considered. Moreover, for some applications (like XUV time-resolved holography) the mirrors have to be placed in the focused beam [10,12] and the intensity on the optics can reach a value of  $10^{14}$  W/cm<sup>2</sup>. Under such conditions the optical properties of the reflecting elements could be changed already during the pulse and the mirror would fail to work [13,14]. These two effects, permanent damage of the coatings and change of the optical properties of materials under high intensity XUV irradiation, can limit the performance of the multilayer optics. The goal of my work [H1] was to define the physical mechanisms responsible for the radiation damage in Mo/Si multilayer systems exposed to an intense ultrashort pulse. In the following paragraph I present the studied sample, performed experiments - single pulse exposures at FLASH facility including time resolved optical microscopy studies, discussion of the results of sample structural characterization in the frames of the proposed thermodynamical model.

#### Experimental

I investigated a Mo/Si multilayer (ML) coating, deposited on superpolished Si substrate, a typical mirror as used for XUV lithography. The multilayer was deposited by e-beam evaporation in a UHV background of  $1 \times 10^{-8}$  mbar, with post-deposition smoothing using low energy ion treatment [15-18]. The multilayer consisted of 50 bilayers of Mo and Si, with a periodicity of 7.96 nm and Mo layer thickness of 40%, optimized for maximum reflectance. The resonant angle and maximum reflectance for p-polarized light were determined to be 29.0 degrees off-normal incidence and 45%, respectively.

The sample was irradiated at the FLASH facility. The radiation wavelength was  $13.5 \pm 0.1$  nm and the XUV pulse duration was  $\sim 10$  fs (FWHM). The sample was at resonant angle with respect to the incident photon beam which was p-polarized. Experimental set-up and alignment procedures were used as described in paper [H4] and section 3.3 above.

I performed XUV reflectivity measurements of the Mo/Si multilayer to study potential changes of the optical properties of the ML coating during the irradiation pulse (on a time scale of a few fs). The measured reflectivity stayed constant (within the experimental uncertainty) over the entire intensity-range investigated, from  $100$  W/cm<sup>2</sup> (measured at synchrotron radiation source) to approximately  $5 \times 10^{13}$  W/cm<sup>2</sup>, corresponding to a fluence of  $500$  mJ/cm<sup>2</sup> irradiations at FLASH facility. This was in agreement with theoretical models, where significant change of the reflectivity of femtosecond duration pulses was predicted only for fluences above  $20$  J/cm<sup>2</sup>, what corresponded to approximately  $2 \times 10^{14}$  W/cm<sup>2</sup>.

I applied the time resolved microscopy technique in the XUV pump – optical probe mode to study the dynamics of the Mo/Si multilayer system. Samples were excited with XUV pulse intensities close to the permanent damage threshold in a single-shot mode [H4]. The optical pulse (probe) delay was fixed at 10 ps, appropriate to examine the initial lattice temperature after relaxation of most of the energy absorbed

by the electron gas to the atoms. Increase of the visible light reflectance in the exited region was observed. The rise of reflectivity had sharp edges which overlapped with the crater border measured a long time after the XUV pulse (after full development of the damage process) using the same microscope. It saturated in the crater center at the maximum value  $35\% \pm 5\%$  larger than the reference outside the irradiation spot. The threshold behavior of the reflectance indicated that its rise was caused by an abrupt change of the optical properties of at least one of the materials. The detailed analysis of the experimental data together with simulations of the sample's reflectivity implied that melting of the amorphous silicon layers at a time scale shorter than 10 ps occurred for fluences above the permanent damage threshold.

Next, the detailed analysis of the morphological and structural changes under irradiations with single femtosecond XUV pulses was performed. From each irradiated spot an image was made with an DIC microscope. Surface modifications could be observed but only for spots irradiated at pulse fluence above threshold value. The damage threshold had been determined to the value of  $45 \pm 7 \text{ mJ/cm}^2$ . The morphology of the Mo/Si multilayer surface after irradiation was further investigated with atomic force microscopy. For fluences between 45 and  $125 \text{ mJ/cm}^2$  a smooth crater was formed and its area matched the area of the damage observed with the interference-polarizing optical microscope. The crater depth ranged from a few nanometers for fluences just above damage threshold up to 68 nm for fluences of approximately  $\sim 125 \text{ mJ/cm}^2$ .

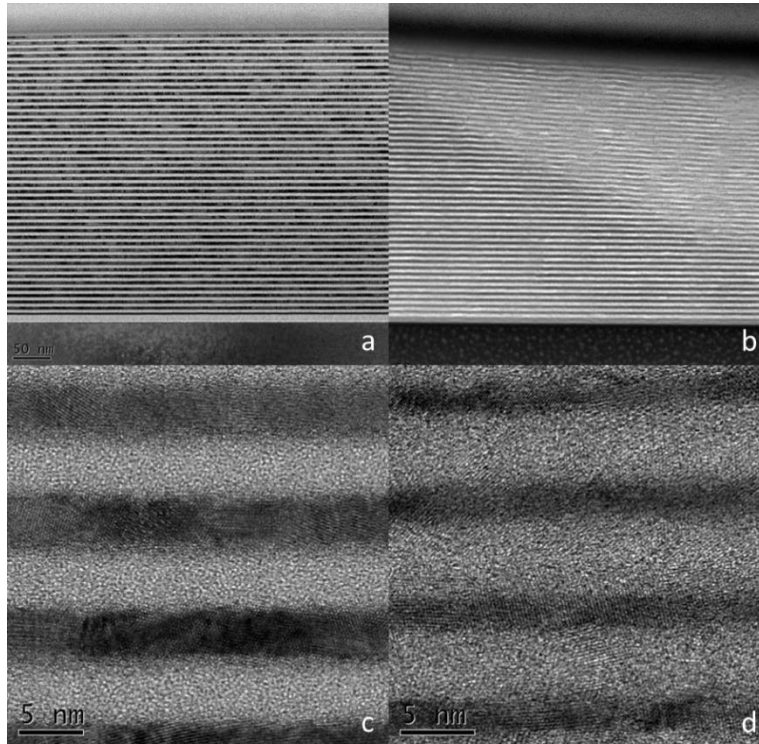


**Figure 7** STEM images of different spots along the crater cross-section. The undamaged region is shown in (a) and (c), the damaged region in (b) and (d). Images (a), and (b) were taken in dark field mode (the darker the image, the lower the density), images (c) and (d) in bright field mode. Figure adapted from [H1].

I used scanning transmission electron microscopy (STEM) to study the structural changes below the crater surface. The results are shown in Figure 7. The analysis of the STEM together with energy-dispersive X-ray spectroscopy (EDX), showed that, two regions could be distinguished: undamaged multilayer, and a fully polycrystalline region where the Mo layers were considerably thinner than the initial ones. In Figure 7(a) and (c) the undamaged region is shown. A clear layer structure could be seen

with sharp interfaces between the polycrystalline Mo and amorphous Si layers. In Figure 7(b) an apparent border, similar to the one observed in AFM and optical microscopy pictures, separating the undamaged and the damaged region is shown. The magnified image of the damaged region is presented in Figure 7(d). The polycrystalline / amorphous layer structure is abruptly changed into the fully polycrystalline layers, with the thickness of Mo being just a fraction of its thickness in the undamaged region, clearly indicating large layer interdiffusion and subsequent (polycrystalline) silicide formation.

## Discussion

All the experimental data obtained by me indicated that the leading damage mechanism for Mo/Si multilayer coating, irradiated with intense femtosecond XUV radiation, was molybdenum silicide formation at the interfaces. This process had been observed previously in dedicated thermal annealing experiments. In such experiments, if the sample was heated to 600 K, the timescale of the diffusion process leading to almost complete intermixing of the layers was typically several hours [19-22], while at approximately 900 K it was measured to be shorter than a minute. However the timescale of diffusion in my pulse heating experiments were different. Silicide formation could only take place if molybdenum or silicon atoms diffuse through the interface. The atomic interdiffusivity through the interfaces of a Mo/Si multilayer ( $D$ ) is  $(4\pm 2)\times 10^{-4}$  nm<sup>2</sup>/s at 530°C, and from Arrhenius's law, approximately  $1.5\times 10^{-3}$  nm<sup>2</sup>/s just below the melting temperature of silicon [23]. I estimated the effect of atomic diffusion in case the sample was heated up to a temperature slightly below the melting point of amorphous silicon for a very short time. Assuming that the heat conductance to the Si substrate cooled the sample down to room temperature in a time shorter than 1 μs [H5], the diffusion length could be calculated to be  $(4D\times t)^{1/2} = 5\times 10^{-5}$  nm, which is significantly smaller than the size of atoms. Hence, atomic diffusion and therefore silicide-formation could be neglected below the melting temperature of amorphous silicon at this relatively short time scale.

To explain this issue I proposed that the surface of Mo/Si sample was melted in a time shorter than 10 ps after the excitation with the XUV pulse, and at an intensity above the damage threshold, what was later evidenced by the pump and probe data. In liquid silicon, the atomic diffusion coefficient is in the order of  $10^{10}$  nm<sup>2</sup>/s [24] which is ~15 orders of magnitude higher than in the solid phase. In such case the molybdenum atoms could penetrate the entire Si layer from both sides on the time scale of sub-nanoseconds (much shorter than silicon resolidification time) and form a molybdenum silicide. The dependency of silicide-formation on melting implied the threshold behavior of the damage which could be observed in all experimental data, apart from reflectivity measurements that were, obviously, not sensitive to processes occurring on a time scale longer than the XUV pulse duration.

There are various known stoichiometries of molybdenum silicide. The density of all of them is larger than the averaged density of their constituent atoms (pure Mo and Si), resulting in a compaction of the multilayer structure upon silicide formation. The AFM data together with the STEM profile showed that in case of the FLASH irradiated sample the compaction was ~17% (68 nm maximum depth of a crater for 50 bilayers, 7.96 nm thick each). This corresponded to the expected compaction if all silicon atoms were consumed for the formation of a MoSi<sub>2</sub> compound [19], which is the most thermodynamically stable state of all molybdenum silicides [25]. It has a formation enthalpy of -132 kJ/mol and had also been observed to be the final state of silicide-formation in the thermal annealing experiments for similar Mo/Si multilayers.

After the silicides were formed, energy was released due to the negative formation enthalpy of MoSi<sub>2</sub>: the heat of formation of MoSi<sub>2</sub> was high enough to increase the mean temperature in the reaction volume (Mo/Si bilayer) from 620 K to just above the melting temperature of amorphous silicon. It served as an energy reservoir for melting deeper layers (less heated due to radiation absorption) and consequently their transformation into silicides.

I have developed a model enabling to estimate how much energy was needed to create silicides in a given number of bilayers. For that purpose the energy balance was calculated taking into account the absorbed energy profile, the energy released due to silicides formation, the energy needed to heat the

silicon and molybdenum to a-Si melting temperature (including the latent heat of a-Si) and the energy loss due to heat dissipation into the substrate.

I calculated the XUV absorption profile in the multilayer with the use of the optical parameters of Mo and Si. These parameters can, in general, be temperature-dependent. However, as described before, the optical parameters didn't change significantly during the pulse and room-temperature values [26] could be used. Subsequently, I calculated the temperature profile in the multilayer from the heat capacities of Mo and amorphous silicon [27,28], the melting temperature (1250 K [27,29]) and the latent heat (33.7 kJ/mol [30,31]) of amorphous silicon in a thin film.

Because of the heat of formation, silicide-formation would be an almost self-sustained reaction (leading to the transformation of the whole multilayer) already at the threshold fluence if one neglected heat dissipation (transport) to the substrate. But this assumption was not valid in the studied system. Using the heat-capacities of thin film molybdenum, amorphous and liquid silicon [32-38], the ratio of the heat conductivities in two regions: conducting (where temperature is higher than the melting temperature of amorphous silicon) and insulating (solid silicon) was calculated. The dissipated fraction of the energy was directly related to the heat conductivity ratio in both regions. No heat dissipation corresponded to a ratio of 0, while complete absence of heat confinement corresponded to a ratio of 1. In the studied case the heat conductivity ratio was in the range of 0.05-0.15. Consequently, most but not all excess energy was confined in the conducting region (where Si was melted) and was therefore used primarily to melt adjacent silicon layers at the conducting-insulating interface.

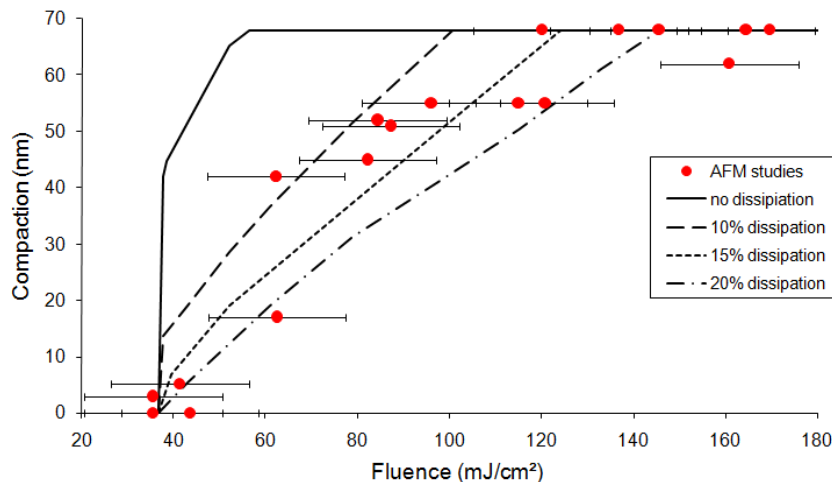


**Figure 8** Compaction as function of fluence. The dots are experimental values obtained from AFM studies. The lines are obtained from thermal dynamic calculations by assuming different dissipation percentages of the excess energy from conducting to insulating region (see detailed description in text). Figure adapted from [H1].

It was assumed that each melted silicon layer was fully transformed into silicides. Since the deposited energy was defined by the incident radiation fluence, and the absolute compaction by the volume of the silicides formed, the fluence dependent compaction of the irradiated multilayer could be calculated. In Figure 8 results of the calculations for different fractions of dissipated energy (0%, 10%, 15% and 20%) are shown. The damage threshold obtained from the calculations for each of the dissipation percentages was the same (lines in Figure 8 cross the x-axis in the same point) and was close (within error bars) to the experimentally obtained value. It showed that energy diffusion was not significant for the single shot damage threshold. However, its effect on the crater profile for fluences above the damage threshold was significant. The predicted crater depth (melting driven compaction) for fluences above the damage threshold varied for different energy losses and the experimental data coincided very well with a narrow range of dissipation percentage from 10% to 20%.

The results showed that standard Mo/Si multilayer optics could be used at the femtosecond XUV light sources for fluences up to  $45 \pm 7 \text{ mJ/cm}^2$  under the condition that the repetition rate of the source allowed the deposited heat to dissipate between subsequent pulses.

### 3.5. Radiation hardness of MoN/SiN multilayer coatings for FEL optics [H2]

#### Introduction

The problem of the physical mechanisms related to the radiation hardness of the multilayer coating for XUV FEL optics was continued in [H2]. To block multilayer damage processes described in [H1], one had to use materials with high melting points and with low diffusion constants, preventing intermixing of the layers. These conditions were fulfilled by MoN/SiN multilayers. They had melting temperatures of the individual layers higher than silicon. Moreover, below the temperature that one of the compounds melted, the atomic diffusion coefficient in MoN/SiN multilayer was 11 orders of magnitude lower than in Mo/Si multilayers [39]. The goal of the work described in [H2] was to determine the damage threshold and the damage mechanism for MoN/SiN multilayers exposed to an intense ultrashort pulse of XUV radiation and compared it to the damage caused by thermal annealing of similar multilayers. In the following paragraph I present the studied sample, performed experiments – thermal annealing of samples and single pulse exposures at FLASH facility, discussion of the results of sample structural characterization in the frames of the proposed thermodynamical model.

#### Experimental

The MoN/SiN multilayer coatings had been deposited on superpolished Si substrates using e-beam evaporation of Mo atoms and magnetron sputtering of Si atoms in a UHV background of  $1 \times 10^{-8}$  mbar, with post-deposition smoothing using low energy ion treatment of the Si layers [16,17,40,41]. Nitridation of the Mo and Si layers was achieved by low energy nitrogen ion treatment during deposition [42-44]. X-ray photo-electron spectroscopy (XPS) was used to qualify the nitridation process. It showed atomic concentration ratios between Mo and N and Si and N that were both equal to  $1 \pm 0.1$ , signifying MoN and SiN formation.

The as-deposited sample was further characterized by means of hard X-ray ( $\lambda = 0.15406 \text{ nm}$ ) and XUV reflectometry. The first technique provided information on the layered structure, including layer thicknesses and multilayer period. The latter technique allowed to determine the multilayer performance, i.e. the angular resolved reflectivity of the multilayer for s-polarized light at 13.5 nm for low (non-destructive) irradiation intensities. The reflectivity at low-intensity (in the order of  $100 \text{ W/cm}^2$ ) was measured at the Center for X-ray Optics (CXRO) at Berkeley. From these measurements, the performance of the multilayer for any polarization and angle could then be predicted by means of simulations with the software package IMD [45]. The multilayer consisted of 40 bilayers of MoN and SiN, with a periodicity of 8.18 nm and a MoN layer thickness of 40% of the total bilayer thickness. The resonant conditions for irradiations at FLASH source - incidence angle of  $28.2 \pm 0.3^\circ$  (off-normal) at p-polarized light and  $13.5 \pm 0.05 \text{ nm}$  wavelength – and corresponding maximum reflectance of 7.7% were determined.

The sample was irradiated in a single-pulse mode at the FLASH facility. The radiation wavelength was  $13.45 \pm 0.05 \text{ nm}$  and the XUV pulse duration was in the order of 10 fs (FWHM). The sample was at resonant angle with respect to the incident photon beam which was p-polarized. Experimental set-up and procedures were used as described above and in [H4].

In order to get better insight in the thermal behavior of the MoN/SiN multilayer, a sample from the same coating run was sequentially thermally annealed at 3 different temperatures. The sample was heated to 773 K, 973 K and 1173 K in a vacuum furnace ( $< 10^{-5}$  mbar). In each step the sample was annealed for a

period of 30 minutes. In order to investigate the structure of the layers, the samples were characterized at each temperature during annealing with wide angle X-ray diffraction (WAXRD) and grazing incidence X-ray reflection (GIXR). In case of the sample annealed at the highest temperature the surface morphology and internal structure were additionally investigated by means of AFM and STEM scans, respectively.

. The reflectivity measurements at middle ( $10^{11}$  W/cm<sup>2</sup> – far away from the focus position) and high intensities ( $5 \times 10^{13}$  W/cm<sup>2</sup>, which corresponded to fluences up to 500 mJ/cm<sup>2</sup>) were performed at FLASH facility. I had shown that, similarly as for Mo/Si ML, the reflectivity is constant, within the experimental uncertainty, over the entire intensity-range investigated. This indicated that the sample damage occurred on timescales longer than the pulse duration.

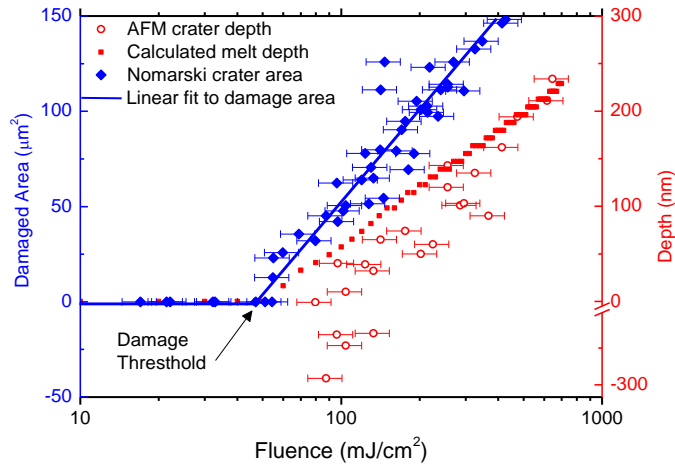


Figure 9 Dependency of the damaged area/depth on the incident beam fluence. The damaged area (blue solid diamonds) was measured by DIC microscopy while the depth of the craters (open red circles) was determined by AFM. The negative values of the AFM correspond to the height of the hills; the depth-axis has been compressed for the negative values. The calculated melt depth (red squares) corresponds to the melting of MoN layers, assuming an averaging of the temperature over each bilayer shortly after energy deposition (see text for details). Figure adapted from [H2].

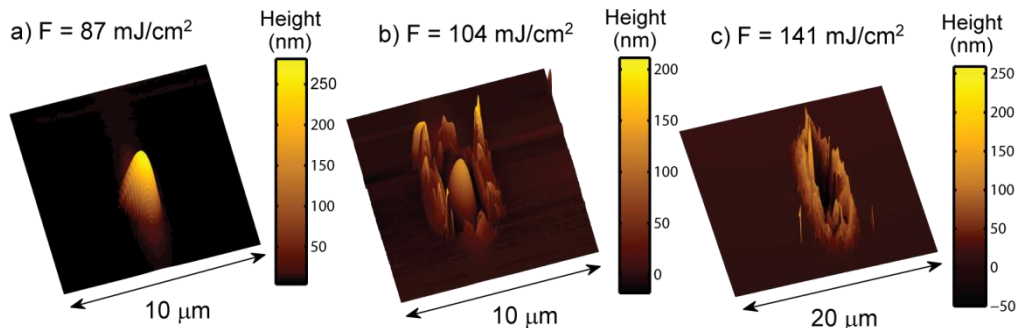


Figure 10 AFM images illustrating the characteristic surface morphology of the multilayer irradiated at three fluence regimes: (a) just above the damage threshold one observes a smooth hill, (b) at intermediate fluences a hill and a crater with side walls can be observed, (c) at high fluences, only a crater with high side walls is observed. Figure adapted from [H2].

Next, the detailed analysis of the morphological and structural changes under irradiations with single femtosecond XUV pulses was performed. The exposed spots were investigated “ex-situ” with different techniques: optical DIC microscopy with Nomarski prism, atomic force microscopy (AFM), scanning electron microscopy (SEM) and, cross-sectional scanning transmission electron microscopy (STEM). From each irradiated spot an image was made with an DIC microscope. Again, a threshold behavior could

be observed with a damage threshold determined [H4] to the value of  $48 \pm 7 \text{ mJ/cm}^2$  (see Figure 9). The morphology of the MoN/SiN multilayer surface after irradiation was further investigated with AFM. Example pictures of three types of observed damage are shown in Figure 10 (a-c). At low fluences, from the damage threshold up to approximately  $100 \text{ mJ/cm}^2$ , smooth hills were formed (Figure 10 (a)). The heights of these hills were between 1 nm and 200 nm. For fluences above  $140 \text{ mJ/cm}^2$ , a crater was formed surrounded by side walls (Figure 10 (c)). In contrast to the very smooth surface of the hill in the first stages of damage, the wall structure was very rough. In some of the irradiated spots a small hill of about 10 nm height was observed at the bottom of the crater. In an intermediate intensity region, for fluences between 100 and  $140 \text{ mJ/cm}^2$  the damage spot consisted of a large hill ( $>100 \text{ nm}$ ), which was surrounded by a small side wall (Figure 10 (b)).

One of the spots, exposed to a fluence of  $141 \text{ mJ/cm}^2$  (the same as presented in Figure 10 (c)), I had further studied by scanning electron microscopy. The SEM image (see Figure 11) showed that on the edge of the crater many semidetached layers were stacked over each other. They formed the wall observed in the AFM map in Figure 10 (c).

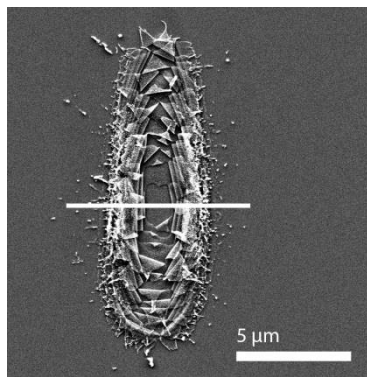


Figure 11 SEM picture of the crater formed by irradiation with a fluence of  $141 \text{ mJ/cm}^2$ . The crater is surrounded by partially detached layers positioned over each other. The white line indicates the location for the cross-section STEM pictures in Figure 12. Figure adapted from [H2].

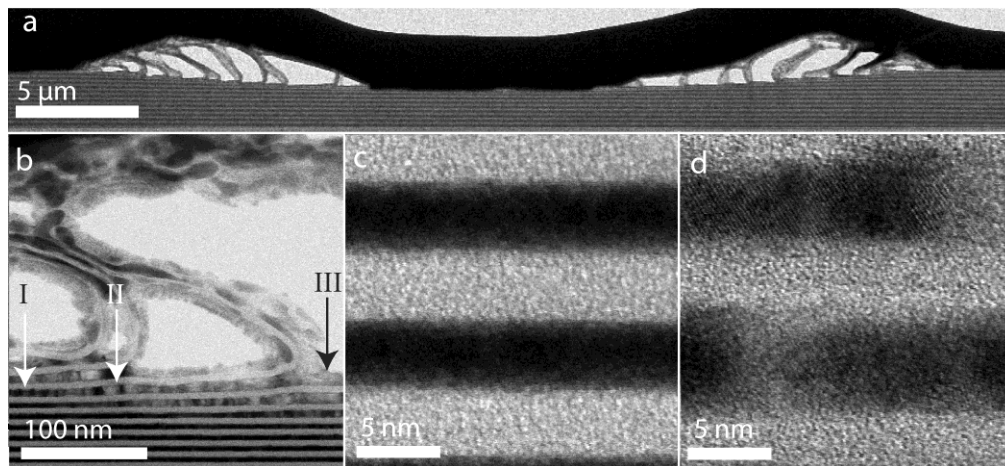


Figure 12 STEM images of the sample cross-section below the irradiated spot: (a) an overview of the crater, (b) magnified image of one of the pillars, (c) and (d) magnified images of the undamaged and the first stages of damage, respectively. The darker areas correspond to MoN and the lighter areas correspond to SiN. On image (b) three regions are marked (see text for details). Figure adapted from [H2].

I used STEM technique to analyze the structural changes below that crater. In Figure 12 (a) an overview image of the crater is shown. The undamaged part of the multilayer could be seen at the bottom of the figure. Above this area one observed structures consisting of pillars of peeled off layers with holes in between (white areas). There was a sharp boundary between the undamaged multilayer and the area where the layers had been peeled off. In Figure 12 (b) a magnified area of one of the pillars is presented. Due to the transversal distribution of the pulse intensity, the absorbed energy density increased from left to right in the picture. At the lowest fluence, at the location indicated by the arrow “I” in Figure 12 (b), no damage could be observed. At increased fluences (at location “II”) new features - light areas in the dark MoN layer appeared. Since STEM was used in the bright field mode, the white areas indicated that the layer had partly crystallized. In addition to the crystallization, the MoN layer also expanded. The expansion continued until the MoN layer completely delaminated from the underlying multilayer, which could be seen at location “III”. Magnified images of the multilayer far away from the crater and in close proximity of the crater are shown on Figure 12 (c) and Figure 12 (d), respectively. The crystallization and expansion of the MoN near the crater could be clearly seen in this comparison. In contrast to the changes observed in the MoN layers after exposure, the SiN layer appeared to stay intact and formed pillars in between the holes.

In order to obtain a better understanding of the thermal behavior of MoN/SiN multilayers, the pristine samples were sequentially annealed at three different temperatures: 773K, 973 K and 1173 K for 30 minutes. After each exposure the crystallinity and the period of the multilayer were determined by WAXRD and GIXR respectively, at a wavelength of 0.15406 nm. From the GIXR spectra, the period of the multilayer at each annealing step was determined by fitting the Bragg peak positions with the modified Bragg law [6]. The results of the WAXRD measurements are shown in Figure 13. The diffraction patterns could be identified as either tetragonal Mo<sub>2</sub>N ( $\beta$ -Mo<sub>2</sub>N) or cubic Mo<sub>2</sub>N ( $\gamma$ -Mo<sub>2</sub>N), as indicated with the dotted lines and the Miller indices on the top of the graph.

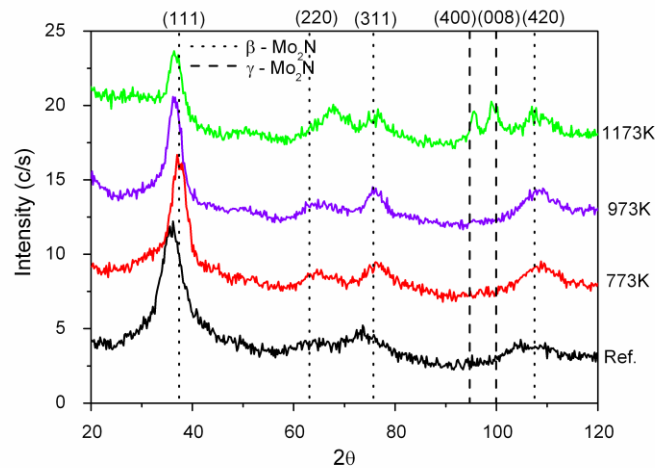


Figure 13 XRD spectra from a MoN/SiN multilayer taken before annealing, and after annealing at 773K, 973K, and 1173K. Every dataset is plotted with an offset of 5 counts for clarity. Figure adapted from [H2].

After annealing to 1173K, AFM investigations showed the formation of hills all over the multilayer surface, which were not present at 773 K and 973 K. I performed further cross-sectional STEM on the multilayer annealed at 1173K. In Figure 14 (a) it is shown that the hills were caused by bubble formation inside the multilayer (I-III). Apart from the bubbles, structural changes were also observed inside the MoN layers, one of which is magnified in Figure 14 (c). They were amorphous and, since they appeared very light in the STEM picture, had a lower density. Most likely these were the onset of the formation of bubbles. At all the other positions in the MoN layers I observed highly ordered crystallites (Figure 14 (b)).

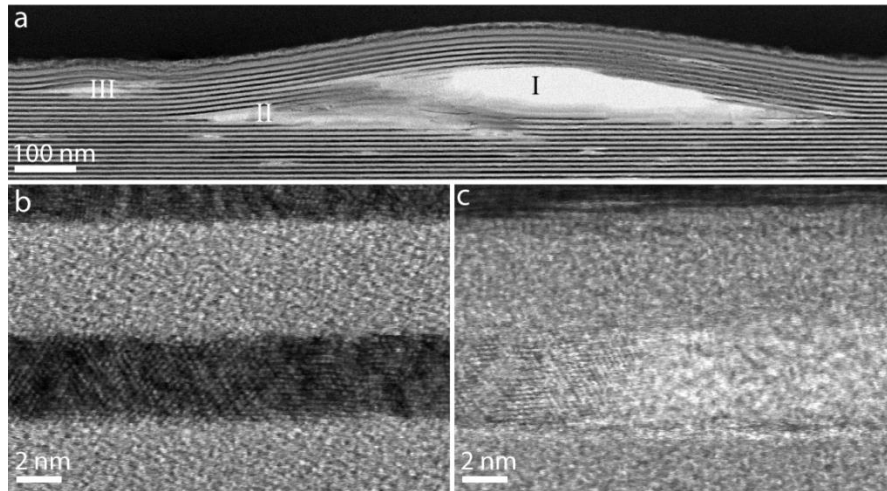


Figure 14 STEM images of the multilayer annealed to 1173K: (a) example of three bubbles, marked with I-III, (b) magnified image of the highly ordered crystalline structure present in most of the MoN layers, (c) magnified image of an amorphous, low density, structure that can be found at various locations in the MoN layers. Figure adapted from [H2].

## Discussion

The as-deposited state of the MoN layers in the studied samples was mostly an amorphous mix of Mo and N atoms in a ratio of 1:1. In between the MoN a small amount of  $\beta$ -Mo<sub>2</sub>N crystals had formed. When the temperature was raised during annealing, the WAXRD spectra showed that the Mo<sub>2</sub>N crystallites increase in size. At 1173 K the pattern of  $\gamma$ -Mo<sub>2</sub>N appeared and the AFM and STEM results revealed bubble formation in the structure. The Gibbs free energy of Mo<sub>2</sub>N formation in the reaction  $Mo(s) + N_2(g) \leftrightarrow Mo_2N(s)$  for an N<sub>2</sub> pressure of 1 bar can be written as [46]:

$$\Delta G_{Mo_2N}^0 = -57320 + 53.89T, \quad (1)$$

where  $\Delta G_{Mo_2N}^0$  is expressed in J/mol and  $T$  is the temperature in Kelvin. Mo<sub>2</sub>N formation was energetically favorable up to the (dissociation) temperature of 1063 K [28]. This temperature could increase with increasing pressure or concentration of N<sub>2</sub> [46]. In the annealing experiment at 773 K and 973 K, below the dissociation temperature, Mo<sub>2</sub>N crystals were formed. After annealing to 1163K, well above the dissociation temperature, the Mo<sub>2</sub>N crystallites started to dissociate into Mo and N<sub>2</sub> gas. This process saturated due to the increase of the unbound nitrogen concentration. However, as observed in the STEM images, at some positions the dissociation process led to formation of volumes of clearly lower density due to a small amount of released N<sub>2</sub> gas. They were the onsets of the bubble formation. At some of them, where there was a “weak point” in the multilayer structure, the MoN layer broke apart and the SiN layers delaminated, what led to the final formation of bubbles. The development of a bubble decreased the N<sub>2</sub> concentration and more gas could be released due to the further dissociation.

Based on the above described model for annealed sample I proposed the following explanation for the experimental data obtained during irradiations at FLASH. Any damage or significant crystallization below the melting point of MoN could be observed. Similarly to the case of the Mo/Si multilayer, atoms simply did not have enough mobility in the solid phase and could not move over significant distances in the short period that the irradiated area was at an enhanced temperature (it could be assumed that the heat conductance to the Si substrate cooled the sample down to room temperature in a time shorter than 1  $\mu$ s). Above the melting point of MoN, atoms were much more mobile in the liquid MoN phase. STEM images showed, crystals were formed at the edge of the melted area and bubbles developed within. In line with the annealing results, it was likely that the Mo<sub>2</sub>N crystals were formed and N<sub>2</sub> gas was released what

leded to bubble formation. However, at the temperatures and multilayer composition used in this study, the phase diagram was not well known [46,47]. Therefore, the mechanisms of the formation of the  $N_2$  bubbles and the  $Mo_2N$  crystals inside the MoN layers could not be determined with absolute certainty. I proposed a model with melting of MoN layer followed by its solidification in  $Mo_2N$  due to heat dissipation to the substrate as a starting point. I presumed that the dissociation of  $Mo_2N$  could not occur due to the very high concentration of nitrogen, higher than the eutectic concentration. Due to the difference in stoichiometry between the  $Mo_2N$  crystals and molten MoN phase the extra nitrogen had to be released. Since the solvability of the nitrogen in liquid MoN was much higher than in  $Mo_2N$ , the  $N_2$  was pushed away from crystals and dissolved in liquid. Thus in the final state, after cooling, there were  $Mo_2N$  crystals surrounded by gaseous  $N_2$ . The more time the solidification process took, the bigger crystals were formed (in Figure 12 (b) the crystal size increased with increasing initial temperature). At the same time the concentration of  $N_2$  in the liquid increased, which resulted in higher pressure in the bubbles after the solidification process ended. Since the main direction of the heat dissipation was towards the substrate, the deeper layers needed less time to solidify what explained formation of small crystals below the crater (see Figure 12 (b)). At the final state, the SiN layers had delaminated due to strain related to the pressure of released  $N_2$  gas. At fluences just above the damage threshold, the SiN layer stayed intact on top of the bubble (Figure 12), at higher fluences, more  $N_2$  was released, therefore the pressure on the SiN layers exceeded the threshold value and the bubble ‘burst’ while the SiN layers fall back on the substrate and formed a wall around the crater (Figure 11 and Figure 12).

To further explore the mechanisms responsible for the damage observed at FLASH facility, I addressed thermal aspects directly after exposure. The depth profile of the energy deposited (absorbed radiation) in the multilayer was calculated as a function of the radiation fluence, similarly as in [H1]. Due to non-uniform energy absorption in the multilayer, the initial temperature was unequally distributed over the bilayers, with maxima in the MoN layers. However, strong temperature gradients and heat exchange between the layers, caused the temperature profile to get smoothed very rapidly. This process was much faster than the heat dissipation to the substrate, due to the difference in the temperature gradient in these two processes. Therefore, it might be considered that shortly after the pulse the temperature was approximately constant over the entire bilayer. The corresponding temperature profile could be calculated from the deposited energy density (averaged over each bilayer) and thermodynamical properties of the materials. The calculated temperature could be compared with the melting temperature of each material - the melting temperatures of both MoN and  $Si_3N_4$  were known from literature [28] to be 2023 K and 2173 K respectively. The layers which temperature raised above that threshold were considered to melt after irradiation and the melted depth (number of bilayers in which MoN is melted) could be calculated.

In Figure 9 (red solid squares) the calculated position of the deepest molten MoN layer as a function of pulse fluence is presented. It was correlated with the depth of the craters as measured by AFM (see Figure 10), assuming delamination of all the molten layers. The data corresponded to each other for fluences above  $300 \text{ mJ/cm}^2$ . For lower fluences the AFM measured crater depths were lower than the calculated molten depths. This difference could be partly explained by an underestimation of the crater depth for low fluences caused by the hills observed in the center of the crater. Moreover, the STEM data showed that one or two layers below the crater did not delaminate and only crystallites were formed within them after irradiation. However the DIC technique was sensitive not only to morphological changes of the material (as AFM) but also structural ones, including formation of the crystallized MoN layer. The damage threshold found from the optical microscopic studies (marked blue on Figure 9) was approximately the same as the melting threshold resulting from the simulations.

Finally I compared the results for MoN/SiN multilayers to those of Mo/Si multilayers. It was remarkable for the MoN/SiN structure of the multilayer the damage threshold ( $48 \pm 7 \text{ mJ/cm}^2$ ) was almost the same as that of Mo/Si multilayer ( $45 \pm 7 \text{ mJ/cm}^2$ ), reported in [H1]. The reflection of the Mo/Si multilayer was  $42 \pm 1\%$ , the reflectance of the MoN/SiN multilayer was  $7 \pm 1\%$ . The lower reflectance leded to enhanced absorption in the presently studied case, which caused the temperatures in the materials to be higher. Therefore, the increased melting temperature of MoN and SiN compared to the one

of Si was not sufficient to increase the damage threshold. On the other hand the decreased atomic diffusivity [39] in the studied sample below the melting temperature increased the critical temperature in the annealing experiment, compared to the Mo/Si multilayer. Thus, I concluded that compared to Mo/Si multilayer the MoN/SiN coatings were expected to have higher damage threshold when expressed as a function of temperature for relatively slow heating processes, but a similar single shot damage threshold in terms of laser energy.

### **3.6. Modeling single shot damage thresholds of multilayer optics for high-intensity short-wavelength radiation sources [H5]**

#### **Introduction**

In the previous chapters I have described results of studies of the physical processes leading to damage of the multilayer optical coatings irradiated with femtosecond XUV pulses of the FLASH FEL source. Systematic experimental studies on damage by high-intensity sources, however, are scarce due to the limited access to such sources, related to the very high costs of beamtime. For that reason in the following chapter I describe application of the multilayer damage model I proposed for comparison of radiation hardness of several multilayer material combinations. For the studies, materials commonly used for multilayer optics as well as new material combinations that are appropriate for short wavelengths in the XUV and soft X-ray ranges (SXR) were selected. In this work, selection criteria placed priority on increasing the damage threshold rather than on optimizing the reflectance. The results are important for optimizing the design of optics for current and future short-wavelength radiation sources.

#### **Model**

I developed a model allowing to estimate the multilayer damage threshold of multilayer optics under irradiation with ultrashort short-wavelength pulses. It was based on the experimental data and theoretical explanations presented in [H1, H2] and was summarizing these results.

The incident radiation was primarily absorbed by electrons in the multilayer structure. The locally deposited energy density was proportional to the product of the local field intensity, the real part of the refractive index, and the absorption coefficient. In a typical situation, the depth profile of the absorbed energy density was non-uniform with local maxima in the reflector layers (e.g. Mo and MoN layers in Mo/Si and MoN/SiN multilayers, respectively). The maximum absorbed energy density at the sample surface corresponded to the resonant irradiation conditions with maximum reflectance. Excited photoelectrons, with kinetic energies in the order of tens or hundreds eV, had a mean free path that was in the order of a few Angstroms [48] and ballistic transport of energy occurred on a length scale equal to the thickness of up to a few bilayers. Secondary electrons were excited by photoelectrons, due to Auger electron emission and impact ionization. Their energy was lower than that of the primary electrons and their mean free path was also smaller, which resulted in a minor energy transport range. Due to the energy exchange between excited electrons, the electron population thermalized at elevated temperatures. This happened on a time scale of 100s fs. Further energy transport could be described by thermal diffusion in the electron gas. The large temperature difference between the consecutive layers on a very short length scale (single layer thickness) created very large temperature gradients, which made the diffusive energy transport very fast. In contrast, the mean temperature gradient over the full multilayer structure and substrate was much lower and corresponded to the exponential decay of the absorbed energy density. The energy transfer on this length scale was much slower (orders of magnitude). One could assume that it was not significant on a time shorter than the time scale of the heat exchange between the electron population

and atoms. This happened on a time scale of picoseconds and led to the increase of the atoms temperature and decrease of electron temperatures, until they (locally) equalized. Such a state I considered as the initial state for calculation in the model. It was characterized by a smooth temperature profile, which was the same for the electrons and the lattice over the full multilayer and substrate structure. Since the thickness of the bilayers was much smaller than the length scale of the exponential decay of the absorbed energy density, each bilayer was assumed to have a flat temperature profile that could be estimated from the deposited energy density averaged over each bilayer and the temperature dependent enthalpy of the materials.

In case of single-pulse irradiations, the process of energy dissipation into the substrate cooled down the sample to the room temperature on a microsecond time scale. In a solid material this was too fast for the atoms to move significantly and to influence the interfaces or the layer structure. However, in a melted material, the atomic diffusivity was enhanced by many orders of magnitude as compared to a solid – 13 orders of magnitude in liquid silicon ( $10^{10}$  nm<sup>2</sup>/s in liquid silicon compared to  $10^{-3}$  nm<sup>2</sup>/s in solid silicon, just below the melting temperature), for example. In the case of melted material, atomic inter-diffusion could occur on a nanosecond time scale, before the melted layers solidified. As a result the structure of the multilayer coating was disturbed, either due to decreased interface sharpness, or to complete destruction of the layer structure. This led to the loss of reflectance (partially or completely, respectively). Both situations I considered as damage of the multilayer structure. Thus, the model-predicted damage threshold was the radiation fluence for which the average temperature in the top bilayer equaled the melting temperature of one of the bilayer materials.

## **Discussion**

The model was applied to materials applicable for multilayer optics in the “water window” range. Damage thresholds of multilayer optics, deposited on a crystalline Si substrate were calculated. The calculations were based on the optical constants, material constants (molar mass, density and melting temperature) and the temperature dependent enthalpy of Li, Li<sub>2</sub>O, B, B<sub>4</sub>C, a-C, a-Si, Si, SiC, Si<sub>3</sub>N<sub>4</sub>, Sc, Ti, V, Cr, Fe, Co, CoO, Ni, NiO, Cu, Mo, Mo<sub>2</sub>B<sub>5</sub>, Mo<sub>2</sub>C, Ru, Sb, La, W and Pt [32,49]. To enable the comparison due to the limitations of the available data I made several assumptions, described below.

Coatings consisting of 600 bilayers were considered because deposition of such stacks had been demonstrated to be experimentally achievable [50]. In the model, the maximum reflectance and damage thresholds as a function of photon energy in the range of 60–620 eV (20 to 2 nm wavelengths) were calculated. The normal incident of the light pulses was considered, while the multilayer optic was considered to have an optimized period,  $d$ , so that the well-known modified Bragg’s law was satisfied [51,52].

Due to the incomplete thermodynamical data and their dependency on the materials deposition method, the melting temperature of bulk materials were applied to the very thin layers in the multilayers. Furthermore, with the exception of a-C and a-Si, all materials were assumed to be crystalline, since no enthalpy values of amorphous materials were available. To give an illustration of the difference in damage threshold values for multilayers containing crystalline or amorphous layers, Mo/Si multilayers having different properties of the silicon layers were compared. In the calculations, the influence on the damage threshold of individual parameters: the melting temperature, the temperature dependent enthalpy, and the optical constants was checked. Substituting the optical constants of crystalline Si to that of amorphous Si had no effect on the damage threshold. Substituting the enthalpy of crystalline Si to that of amorphous Si, the damage threshold was increased by approximately 6%. Finally, when changing the melting temperature from 1687 K (crystalline Si) to 1250 K (amorphous Si), the damage threshold was decreased by approximately 34%.

In the model, it had been assumed that there was no interface diffusion or roughness ( $\sigma = 0$  nm) hence, no compound formation was taken into account. This simplified the modelling and comparison between different systems, while also providing the most accurate damage threshold predictions. The latter was

often true because damage was caused by melting, so compound formation could only reduce the damage threshold if the compound had a lower melting temperature than its components.

In case of the multilayers containing amorphous carbon, I have proposed that permanent damage might occur at temperatures below melting point. In one of my other works [P27], it was shown that a 40 nm thick amorphous carbon layer would crystallize when irradiated by femtosecond 830 eV X-ray FEL pulses. This graphitization was observed to occur at 1050 K, much below the melting temperature (3900 K) of carbon, what is related to the short length scale of required atomic rearrangement. If one assumed that, at photon energies below the carbon absorption edge, this phase transition occurred also at 1050 K, then the values of the calculated damage threshold became drastically lowered than in a melting case.

Due to the restrictions mentioned above, studies of the multilayer optical damage thresholds were, in the first instance qualitative. Nevertheless, they represented the first investigation of this kind and provided new candidate multilayer systems that offered promise for optics suitable for high-intensity short-wavelength radiation sources.

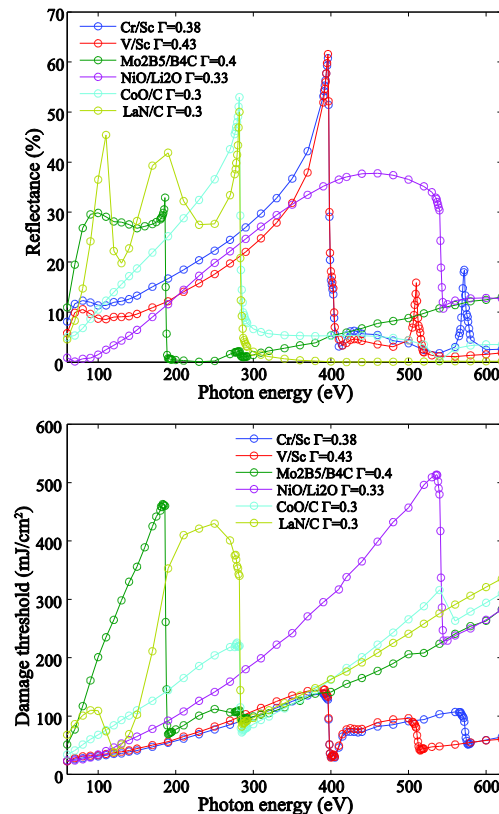


Figure 15 Reflectance and damage threshold for several multilayers optimized for photon energies below different absorption edges and the water window. Figure adapted from [H3].

Based on the above presented model four groups of multilayer coatings had been tested: optimized for wavelengths below the boron absorption edge (188 eV), the carbon edge (284 eV), the scandium edge (420 eV), and in the whole water window (284 – 532 eV). The general selection criteria were given by (1) high refractive index contrast between the consecutive layers in a bilayer (reflector and spacer layers), (2) low extinction coefficients, (3) low miscibility between the material pairs, i.e., low interdiffusivity and low chemical reactivity, (4) smooth and continuous growth properties, and (5) ease of use. Ease of use was determined by availability, and health and safety concerns [51]. Besides the highest achievable

reflectance also bandwidth, stress and lifetime (long term thermal stability) were considered important for most applications.

As an overview, the most interesting multilayer combinations are displayed in Figure 15, which shows the theoretical maximum reflectance and the calculated damage thresholds as a function of the photon energy in the range of 60 to 620 eV. For the boron edge the most promising multilayer with high damage threshold was Mo<sub>2</sub>B<sub>5</sub>/B<sub>4</sub>C, however, LaN/B<sub>4</sub>C was also expected to have a high damage threshold. For the carbon edge, CoO/C appeared to be a good alternative to Co/C and V/C, while LaN/C was also promising. For the scandium (and vanadium) absorption edge the use V/Sc instead of the commonly used Cr/Sc was proposed. Furthermore, as an alternative for currently used multilayer systems with limited performance in the water window, new material combinations that use Li<sub>2</sub>O as a spacer material were proposed.

Investigations in [H3] demonstrated that the damage threshold of multilayers can vary over a large range, from several to hundreds of mJ/cm<sup>2</sup>. This finding also allowed to conclude that multilayer mirrors are serious candidates for damage resistant optics.

### **3.7. The role of heat accumulation on the multi-shot damage of silicon irradiated with femtosecond XUV pulses at a 1 MHz repetition rate.**

#### **Introduction**

Studies of physical processes leading to the damage of multilayer optical coatings were performed for the case of single-pulse irradiations, defining upper limit for the optics radiation hardness – a single shot damage threshold. However structural changes can be induced in optics below this limit in case of irradiations with series of pulses of high mean power density due to the heat accumulation. FEL sources based on superconducting accelerating technology are especially suitable for studies in a multi-shot mode of operation, in which the sample is exposed to a number of pulses at the same spot. FLASH source provides up to 800 XUV pulses of 10-100 fs each with a 1 MHz repetition rate [53]. The pulse spacing of 1 μs is of the order of the typical time constant of the heat dissipation from the solid sample surface to the bulk and is therefore suitable for studying heat accumulation processes. The multi-shot irradiations of solid materials with short-wavelength (ionizing) pulses offers a number of advantages over experiments with sources operating in the optical range. First of all, the energy deposition process is practically undisturbed by optical nonlinearities caused by processes such as multiphoton absorption and free carrier absorption. Moreover the absorption depth can be controlled over orders of magnitude by tuning the FEL to an appropriate wavelength (e.g. just above or below an absorption edge). In particular, ultrashort XUV pulses provide a way to create well-defined excitation conditions in a large sample volume [54]. In such a case the temperature gradients are low and the influence of the heat dissipation processes is sustained. Using FELs, it became possible to significantly extend the optical studies of phase transitions by systematic studies of transition dynamics, energy transfer, and accumulation processes of heat and damage.

Among the many materials studied regarding their structural modifications and damage, silicon plays a significant role, since it is treated as a reference material (it is relatively easily accessible and its physical properties are well known) and due to its fundamental importance for electronics and optics. A lot of work on this subject had been particularly done using a wide range of optical lasers with different emission characteristics, wavelength (from microwaves to VUV), pulse length (from femtoseconds to microseconds, and CW), repetition rate, and intensity (see [55] for review). For silicon, the phase transition mechanisms induced with a single femtosecond and monochromatic pulse of wavelength in the range of XUV and X-ray were studied previously, mostly for the angle of incidence close to surface normal. Silicon in the form of bulk crystals [P7, P12-P14, P20] [56-58] and amorphous layers in Si/C [P15] and Mo/Si multilayer systems [H1] had been examined with single femtosecond pulses of short-

wavelength radiation. These measurements had shown that the single shot structural modifications were caused by melting. I extended the studies of the phase transitions in silicon, induced by femtosecond XUV pulses, to investigation of heat accumulation on damage in case of the multi-shot irradiations with a high repetition rate (1 MHz). In the following paragraph I present performed experiments – multiple pulse exposures of silicon at FLASH facility, and discussion of sample structural modifications in the frames of the proposed thermodynamical model.

### **Experiment**

A bulk, (001)-oriented, silicon single crystal with a super-polished top surface was used in this study. The sample was found to have a surface roughness smaller than 0.2 nm (RMS) measured by X-ray reflectometry and atomic force microscopy. I conducted the experiment at the FLASH source using standard methods and experimental techniques for FEL damage studies described in [H4]. The samples were exposed to femtosecond XUV radiation, the wavelength was centered at 13.5 nm. The incidence angle was 15.5 degrees off normal. Pulse duration was approximately 100 fs (FWHM). Each irradiated spot was accumulating a train of 400 single pulses with a 1 MHz repetition rate. Pulse energies for a given spot varied by approximately  $\pm 20\%$  from a trend line (averaged over many pulse trains). Total variation of the energy deposited at each spot from a mean value was approximately  $\pm 40\%$ . Maximum beam fluence was reduced to  $64 \text{ mJ/cm}^2$  - well below the single-pulse surface modification threshold fluence (approximately  $410 \text{ mJ/cm}^2$ , see below). Therefore the mixing of single and multi-shot irradiation conditions which could influence the path of the structural modification was avoided. After irradiations, I investigated the spots by optical DIC microscopy with Nomarski prism and scanning electron microscopy (SEM). I also studied sample cross-sections at selected positions inside the irradiated spot by means of the TEM technique.

For comparison, I irradiated the same silicon sample with 4000 and 400 pulses at a 10 Hz repetition rate (accumulated single pulses instead of pulse trains). The mean fluence of accumulated pulses was up to  $43 \text{ mJ/cm}^2$ , a higher value than the surface modification thresholds for a 1 MHz repetition rate. In this case, no surface modifications in the exposed spots were observed by means of DIC microscopy.

The single shot melting threshold was not directly determined for irradiation at a 13.5 nm wavelength at normal incidence. Instead, I estimated it to be  $410 \text{ mJ/cm}^2$ , from the experimental values obtained for irradiations at the wavelength of 32.5 nm [P12,P14] and 0.124 nm (10 keV photon energy) [57,58] and the theoretical predictions [59].

### **Simulations**

The experimental studies of multi-shot irradiations of Si with intense XUV pulses at 1 MHz repetition rate were supported by theoretical modelling. I simulated heat accumulation and transport by means of a simple 1-D heat diffusion model. I solved the problem using the enthalpy method [60] in which the evolution of the latent heat was accounted for by the enthalpy as well as the relationship between the enthalpy and temperature. I made the following assumptions. A simple 1-D geometry of the sample, where the temperature and enthalpy was uniform over planes parallel to the sample surface and varied only in the perpendicular direction (in depth), was used. This was justified by the fact that the effective XUV beam spot diameter during the experiment was in the order of 300 micrometers, and therefore all temperature/enthalpy gradients were much smaller in the lateral direction than in-depth. In this case the heat diffusion problem could be expressed by the following equation:

$$\frac{\partial h}{\partial t} = \frac{\partial}{\partial x} \left( \frac{k}{c} \frac{\partial h}{\partial x} \right) + S, \quad (1)$$

where  $h$  was the local enthalpy of the sample depending on spatial ( $x$ ) and time ( $t$ ) variables,  $k$  was the total (sum of electron and phonon) heat conductivity,  $C$  was the heat capacity, and  $S$  was the source term. The relationship between the enthalpy and temperature was found in [61], while the  $k/C$  ratio dependence on the enthalpy was calculated based on data provided in [62]. The enthalpy scale could be divided into three regions: for  $h$  lower than approximately  $3.0 \text{ GJ/m}^3$  when the temperature stayed below the melting temperature  $T_{\text{melt}} = 1683 \text{ K}$ ,  $h$  between approximately  $3.0$  and  $7.17 \text{ GJ/m}^3$ , when the temperature stayed constant at the  $T_{\text{melt}}$  for all enthalpy values, and for  $h$  above  $7.17 \text{ GJ/m}^3$ , when sample was liquid (change into gas phase was not considered in my studies). When the temperature was equal to  $T_{\text{melt}}$ , the heat capacity tended to infinity (as temperature remains constant while one adds heat to the system) and  $k/C$  was equal to zero.

The source term,  $S$ , corresponded to the absorption of radiation. Its depth dependence was proportional to the exponential absorption term  $\sim \exp(-x/L_{\text{abs}})$  following D'Alembert law with  $L_{\text{abs}}$  equal to  $568.5 \text{ nm}$  (radiation penetration depth at a  $13.5 \text{ nm}$  wavelength and incidence angle of  $15.5^\circ$ , based on [26]). The sample thickness was taken in the calculations as  $900 \text{ }\mu\text{m}$ . I assumed that there is no heat transfer at the sample boundaries. The observed temperature rise on the back of the sample surface was less than  $1 \text{ K}$  for all simulations. The initial value of the enthalpy in the sample was taken as zero ( $h(x)=0$  for all  $x$ ), and the temperature of the sample as  $298 \text{ K}$ . Although the pulse duration was approximately  $100 \text{ fs}$ , the time scale of the source term (modeled by one period of a  $\sin^2$  function) was set to  $2 \text{ ps}$ . This corresponded to the characteristic electron-phonon coupling time constant representing the time needed to transfer the energy absorbed by electrons to the lattice [63]. The maximum power density of the source term ( $p$ ) was a function of the radiation fluence ( $F$ ), sample reflectivity ( $R \approx 0$ ), and  $L_{\text{abs}}$ :  $p = (1-R) \times F/L_{\text{abs}}$ . Due to relatively small temperature gradients in the investigated system, determined mostly by the radiation penetration depth, the energy diffusion by the electron gas before its thermalization with the lattice was neglected. I calculated the multi-shot irradiations in the following sequence. First, the heat diffusion equation was solved for a  $1 \text{ }\mu\text{s}$  period, i.e. the time between the successive laser pulses. Next, the final state of calculations for the first pulse was taken as an initial state for the second pulse. This was repeated the same way in  $1 \text{ }\mu\text{s}$  steps for the given number of pulses. The estimated relative errors of the simulations were approximately  $20\%$  and were associated with the above discussed approximations (1-D geometry, choice of the source term etc.) and the accuracy of the used model parameters (such as heat conductivity dependency on the enthalpy).

## Discussion

I analyzed and interpreted the obtained experimental data. Three types of surface morphological and structural modifications were observed in silicon samples irradiated with  $400 \text{ XUV}$  pulses of approximately  $100 \text{ femtosecond}$  duration at a  $1 \text{ MHz}$  repetition rate. These modifications evidenced a threshold dependency on the mean fluence of the incident pulse train. Above the lowest threshold of  $38 \text{ mJ/cm}^2$ , only surface changes in a form of nano-droplets could be observed (Figure 16 (a) ). My observations suggested that they were formed due to reassembly of a locally molten surface material. The melting occurred only at the sample surface (top few nanometers) and had a lower fluence threshold than that for melting of a bulk material. It might be explained by a lower melting threshold (in terms of enthalpy) of the surface material than the bulk. It depended on the surface structural parameters which were related to the sample's surface polishing. The second threshold of  $40 \text{ mJ/cm}^2$  was related to a formation of a large number of lattice defects in a layer thickness of approximately  $0.5 \text{ }\mu\text{m}$  (see Figure 16 (b)). Such behavior might be explained by the enhanced lattice elasticity when the temperature reaches the melting point. Under such conditions lattice atoms started to dislocate due to thermal movements and broken bonds. As soon as the sample cooled down, the defects got frozen and stayed localized. This process was repeated many times and the number of dislocations developed with the number of irradiating pulses. There were much less defects above the third threshold of  $42 \text{ mJ/cm}^2$  (Figure 16 (c) ). I concluded that under these conditions the sample reached the liquid (amorphous) phase at the end of the pulse train.

One observed material expansion in the center of the spot that could be explained by hydrodynamical movement of the liquid material. The freezing took long enough that the crystalline structure was formed in a quasi-epitaxial process. Some of the dislocations were still frozen but their density was much smaller than dislocations observed originating from the non-liquid state.

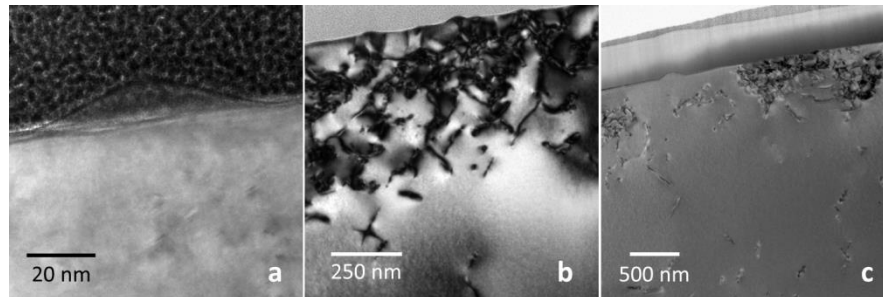


Figure 16 TEM images of the sample cross-sections in three areas: (a) droplet-like surface feature of the region just above the lowest threshold, (b) 0.5  $\mu\text{m}$  thick layer of lattice defects in the vicinity of the sample surface above the middle threshold, (c) lattice defects at position in the vicinity of the highest threshold. A polycrystalline ultrathin Pt cap layer is visible, deposited for the sample protection. Figure adapted from [H5].

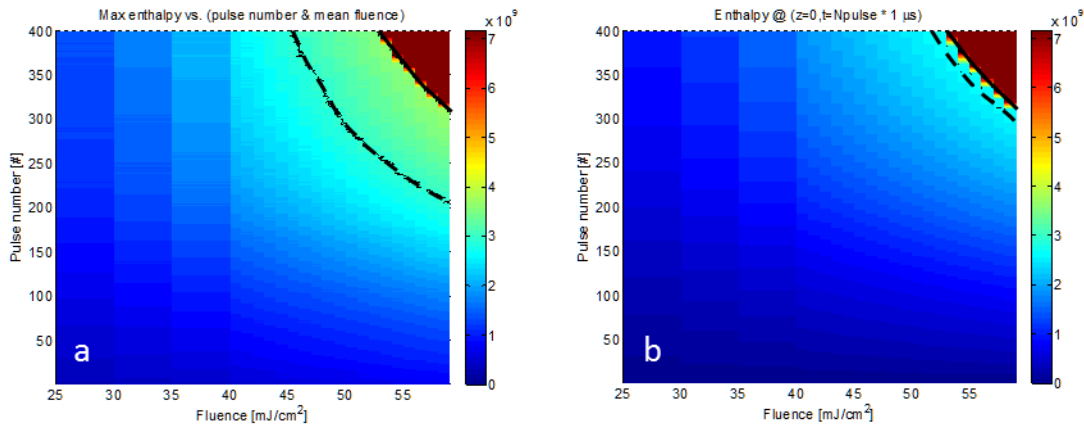


Figure 17 (a) Maximum enthalpy reached after each pulse and (b) accumulated enthalpy before each pulse for various mean fluence levels (x-axis) and number of pulses (y-axis). Two enthalpy levels of 3.0 and 7.17  $\text{GJ/m}^3$  corresponding to  $T=T_{\text{melt}}$  and start of the liquid phase are marked with black lines (dashed and solid, respectively). The color map corresponds to the enthalpy range of 0 to 7.17  $\text{GJ/m}^3$  (liquid sample). Figure adapted from [H5].

I supported the above proposed explanation of the experimental results by the theoretical model described by the heat diffusion equation. I performed simulations of silicon irradiations by a train of 400 pulses at a 1 MHz repetition rate for fluences in the range of 25-60  $\text{mJ/cm}^2$ . The calculations showed that, at the time when the next pulse should arrive, there was still a significant fraction of heat left at the sample surface by the preceding pulse, so heat accumulation had to take place in the multi-shot case. Maximum enthalpy reached for each pulse and accumulated enthalpy before each next pulse was calculated for various mean fluence levels (Figure 17 (a) and (b), respectively). The thresholds for reaching  $T_{\text{melt}}$  (45  $\text{mJ/cm}^2$ ) and the full liquid state (54  $\text{mJ/cm}^2$ ) indeed overlap with the experimental values, within the error bounds. Simulations showed that as soon as the melting temperature was reached, the heat dissipation from the surface slowed down abruptly (due to the lack of temperature gradient at these conditions). Most of the energy of the pulses absorbed after reaching  $T_{\text{melt}}$  did not diffuse from the surface and added to the latent heat of melting at the constant melting temperature. Hence the two thresholds were very close to each other.

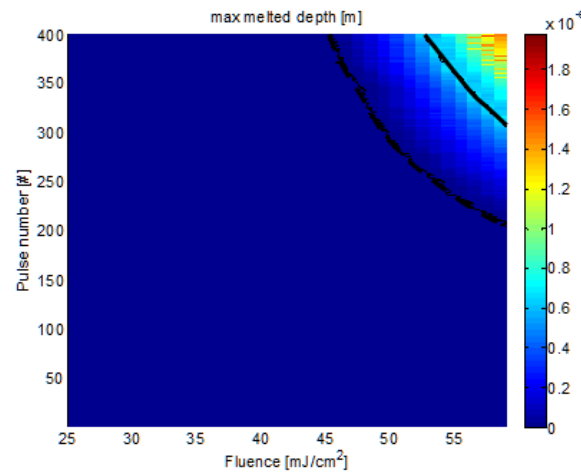


Figure 18 Map of the maximum melted depth after each pulse for various fluence levels (x-axis) and number of pulses (y-axis).. Two enthalpy levels of 3 and 7.17 GJ/m<sup>3</sup> corresponding to  $T=T_{\text{melt}}$  and the start of the liquid phase are marked with black lines (dashed and solid, respectively). The color map corresponds to the depth range of 0 to 2 micrometers. Figure adapted from [H5].

My model supported the explanation of a high density of defects in the top 0.5  $\mu\text{m}$  layer of the sample for fluences above the second threshold fluence, as well. In Figure 18 it is shown that over a similar depth the sample reached the melting temperature but was not yet liquid. For example, just below the third one the sample reached the melting temperature (due to a next pulse absorption) and cooled below it (due to a heat diffusion) for up to  $\sim 150$  times. Since the defect formation was not reversed by an epitaxial growth from the liquid phase, the defect density increased after each pulse.

No surface damage was observed for multi-pulse irradiations with a 10 Hz repetition rate, when the system had enough time (100 ms) for relaxation between pulses. It agreed with the simulations that showed for a single pulse a threshold of 410  $\text{mJ}/\text{cm}^2$  - a value much higher than the maximum fluence of the applied pulses. It indicated that the heat accumulation played an important role in the studied processes. If the delay between subsequent pulses was short enough (in our case, it is 1 microsecond) then there was not enough time for complete heat dissipation from the surface; as a result the heat accumulated.

Apart the fundamental understanding of the multi-shot accumulation processes in silicon, my studies were of practical importance, as well. My research helped to specify geometrical constraints and structural requirements for optical substrates for new short wavelength FEL sources.

### 3.8. Other work related to the scientific achievement.

The publications listed in Appendix 4 Chapter A Section [2] were closely related the scientific achievement but are not included because my contribution was not leading. They are categorized according to the following research fields:

#### Structural phase transitions

Firstly, I have further studied structural phase transitions under irradiations with femtosecond XUV and X-ray pulses in solids. Melting and ablation were investigated at available short wavelength FELs (FLASH, Germany in VUV FEL and SACLA in Japan, LCLS in USA) at various irradiations conditions (photon energy, incidence angle) for various materials. For most of experiments methods described in [H4] were used, while these at FLASH facility were performed using the experimental set-up described in

[H4]. I was one of the leading scientist in most of the experiments and supervised the experimental preparations, participated in the data acquisition and interpretation, took part in writing manuscripts.

In one of the first experiment, time-resolved reflectivity measurements of Si and GaAs surfaces irradiated with intense femtosecond light pulses at 32 nm wavelength supplemented by a postmortem analysis of the induced permanent structural surface modifications were performed [P12] with use of the experimental station described in [H4]. Ejection of molten material was indicated as a main mechanisms for crater formation. Threshold fluences for melting and ablation were experimentally estimated. Distinct differences in the material response compared with femtosecond optical excitation were found. They were attributed to the increased penetration depth of the XUV radiation and the absence of any absorption nonlinearities.

Among the mostly studied were materials of interest to XUV and X-ray optics – B<sub>4</sub>C and SiC. The damage threshold of the samples showed a strong photon energy dependence, however in the range of 38-830 eV were typically on the order of the fluence required for thermal melting [P14, P18, P22]. The damage threshold was higher for bulk materials than for thin (micrometer thick) films. At 38 eV photon energy, for fluences larger than melting threshold, the experimental data suggested that the craters were formed by two-phase vaporization (similarly to the Si and GaAs samples behavior). In case of irradiations of SiC and B<sub>4</sub>C samples at high photon energies (830 eV) at normal incidence strong mechanical cracking in the materials (additional to melting was observed), which may be due to the larger penetration depths of the hard X-rays. In case of irradiations using 7 and 12 keV photon energies at grazing angle below critical angle for the B<sub>4</sub>C and Ru layers the damage threshold dose limits were found to be orders of magnitude higher than would naively be expected based on normal incidence exposures [P31]. The incorporation of energy transport and dissipation via keV level energetic photoelectrons were necessary to explain the observed damage threshold.

Another set of samples important for short-wavelength FEL optics consisted of a-C thin layers on Si substrate and bulk chemical-vapor-deposited carbon (CVD diamond). I participated in experimental and theoretical studies of the structural transition of diamond under an irradiation with an intense femtosecond pulse of 24–275 eV photon energy. Experimental results obtained show that the irradiated diamond undergoes a solid-to-solid phase transition to graphite [P29]. Theoretical findings suggest that the nature of this transition is nonthermal, stimulated by a change of the interatomic potential triggered by the excitation of valence electrons. Ultrashort laser pulse duration enabled to identify the subsequent steps of this process: electron excitation, band gap collapse, and the following atomic motion. A good agreement between the experimentally measured and theoretically calculated damage thresholds for the XUV range supports the conclusions. In case of the a-C samples at normal incidence irradiations at 38 eV the threshold for surface damage was on the order of the fluence required for thermal melting [P14]. However under exposure to femtosecond X-ray free-electron laser pulses at different grazing angles above and below the critical angle for 91.8 and 177.1 eV photons energies [P17, P24] and at normal incidence at 830 eV [P27] a different mechanism of structural changes was observed. Experimental data gave evidence for the solid-solid phase transition – graphitization, similarly as in the case of CVD diamond. The interaction at 830 eV photon energy was modeled by an accurate time-dependent treatment of the ionization dynamics coupled to a two-temperature model. In contrary to the CVD diamond case, the calculated low ionization rate and high atom temperature suggested a thermally activated phase transition for a-C samples. Furthermore, the interaction of free electron laser pulses with grating structure (an example of non-flat sample) was investigated using FEL radiation at 177.1 eV photon energy [P26]. For fluences above threshold values, the interaction triggered a damage process starting at the edge of the grating structure facing the incident radiation as evidenced by optical and atomic force microscopy. Simulations based on solution of the Helmholtz equation demonstrated an enhancement of the electric field intensity

distribution at the edge of the grating structure. It led to a significantly lower transition threshold than in a case of flat samples irradiated at similar conditions.

In contrary to the model applied to multilayers damage, the theoretical explanations for structural changes observed induced by irradiations below ablation threshold provided in the above reported publications took into account only the local changes of the atomic arrangement (melting, solid-solid phase transition) neglecting atomic diffusion over larger length scale and modifications of the chemical composition of the materials.

Furthermore I studied the reflectivity of Si/C multilayers at fluxes up to  $3 \times 10^{14}$  W/cm<sup>2</sup> at 32 nm wavelength [P15]. Even though the nanostructures were ultimately completely destroyed, it was found that they maintained their integrity and reflectance characteristics during the 25 fs-long pulse, with no evidence for any structural changes over lengths greater than 3 Å. This experiment demonstrated that with intense ultrashort pulses, structural damage does not occur during the pulse, giving credence to the concept of diffraction imaging of single macromolecules.

Another investigated research field were synchrotron radiation studies of lateral strain effects in bulk Si induced by irradiations with short-wavelength FEL radiation in high intensity experiments, interesting for target and exposure matrix design [P20, P25, P28, P33]. Silicon crystalline samples were exposed to intense single pulses of FEL radiation (photon energies of 92, 1892 and 2000 eV) what led to melting and ablation of the surface material. The deformation field around craters along the whole thickness of silicon wafers was observed by means of the synchrotron diffraction topography using the beam perpendicular to the surface of the sample. The geometrical shape and depth extension around craters was evaluated based on numerous, dense series of section topographs. The range and shape of the crystal defects connected with craters was approximated as droplet- and rod-like inclusions.

### **Intense XUV and X-ray beam characterization**

Spatial distribution of the FEL radiation fluence was an important property for many experiments, along with duration and total energy of a pulse, photon energy and radiation bandwidth etc. It played an essential role in laser-matter interaction research employing intense non-ideal beams. However this parameter was not easy to measure for intense photon beams in the XUV and X-ray spectral regimes, like at short wavelength FEL sources. In one of the first approaches, described in Chapter 3.3 and [H1], I developed a method to measure the beam profile in case of a multi-gaussian beam (i.e. in case the irradiated spot consisted of a few semi-gaussian parts). Important parameters characterizing the beam - size (area) of each part and corresponding portion of the pulse energies - could be calculated based on this procedure. I participated in continuation of this work for more general case of a non-gaussian beams. In a series of publications [P16, P19, P23, P30, P32] both, an extended theoretical background of so-called fluence scan (f-scan) method and its applications for offline characterization of focused short-wavelength (XUV and X-ray) laser beams were presented. The method exploited ablative imprints in various solids (poly(methyl methacrylate) - PMMA, ionic crystals like Ce:YAG, PbWO<sub>4</sub> etc.) to visualize iso-fluence beam contours at different fluence and/or clip levels.

Furthermore I participated in studies of photoluminescence saturation in monocrystalline cerium doped yttrium aluminum garnet (Ce:YAG) exposed to intense extreme ultraviolet (XUV) and X-ray radiation delivered from three FELs [P37]. The measurements were performed with photon energies of 12.7, 48.4, 92 and 266 eV. Saturation of the photon yield was observed. It was explained by mutual quenching of excitons created at high densities, preceding the stage of energy transfer to the Ce<sup>3+</sup> ions. The results could be used to predict saturation effects in scintillator slabs placed in imaging systems of bright XUV, X-ray and particle beams.

**Structural and magnetic characterization of Pt/Co/Pt trilayers**

I studied an irreversible rotation of magnetization from in-plane to an out-of-plane direction induced in Pt/Co/Pt epitaxial trilayers by nanosecond pulses of extreme ultraviolet radiation and femtosecond optical laser pulses [P34-P36]. Various techniques, including X-ray diffraction, X-ray reflectivity, polarized neutron reflectivity, atomic force microscopy and magneto-optical Kerr effect in polar configuration were used to investigate the properties of the as-grown and irradiated samples. Formation of Co-Pt alloy phase and changes of the lattice strain were demonstrated in irradiated samples and correlated with magnetization changes. In the frame of a project I was a leader of the XUV irradiations and structural characterization of ultrathin Pt/Co/Pt samples.

**3.9. Other activities unrelated to the scientific achievement****Warm Dense Matter studies**

I have participated in experimental studies of Warm Dense Matter (WDM) formation at the FLASH facility [P38-P45]. XUV FEL radiation was focused down to a micrometer spot size with multilayer coated optics at solid targets driving them to highly excited states at densities typical for solids. The properties of such a plasma state formed with intense femtosecond XUV pulses were investigated by means of XUV transmission, XUV and X-ray emission spectroscopy and time-of-flight ion spectroscopy. Saturable absorption of an L-shell transitions in Al at record intensities above  $10^{16}$  W/cm<sup>2</sup> in the XUV spectral range was observed by means of transmission measurements. Immediately after the intense XUV pulse had passed, the sample was in an exotic state where all the aluminum atoms had an L-shell hole, and the valence band had approximately a 9 eV temperature, while the atoms were still on their crystallographic positions. Subsequently, Auger decay heated the material to the WDM regime (at around 25 eV temperatures) - highly relevant to planetary science, astrophysics and inertial confinement fusion. Further studies by means of XUV and X-ray emission spectroscopies had confirmed these observations. They provided information on the electronic temperatures and densities of strongly excited system immediately after the excitation pulse, which were in a good agreement with detailed calculations of the electronic structure, based on finite temperature density functional theory. Furthermore, time-of-flight ion spectroscopy and crater analysis were used to characterize interaction of intense femtosecond XUV radiation (up to  $10^{17}$  W/cm<sup>2</sup>) with Nb and V targets loaded with hydrogen and deuterium. Hot dense plasma with temperatures reaching 400 eV (corresponding to 4.6 million K electronic temperature) was formed. A plasma expansion into vacuum with charge separation ejected ions with kinetic energies reaching 5 keV for protons and deuterons and 20 keV for multiply-ionized metal ions were measured. With increasing power densities saturation effects were observed, related to a transient surface transparency that developed in the sample during the pulse. The studied phenomena were further applied to find a focus position of intense XUV pulses.

In the above presented work I developed the radiation detection system and time-of-flight ion spectrometer, I participated in experimental campaigns and took part in the analysis of the experimental data, I contributed in the preparation of the manuscripts.

**Multilayer optics development**

My other significant activity was development of the multilayer optics. I performed the first quantitative comparison between Total Electron Yield (TEY) and Reconstruction of Attosecond harmonic Burst By Interference in Two photon Transition (RABBITT) techniques for the characterization of the XUV phase shift induced by reflection on a ML mirror [P46] The two techniques are very different and have been implemented on different facilities (synchrotron radiation at BESSY facility for TEY, laser

based high harmonic source at CELIA facility for RABBITT). The results were in excellent agreement, confirming the validity of both approaches. My contribution to this work consisted in general design of the studied multilayer coatings, in the participation in experiments at CELIA facility, analysis and discussion of the results.

Furthermore I have developed and extensively characterized amplitude-division beam splitters for XUV radiation sources [P47]. Mo/Si multilayer coatings were deposited on 50 nm-thick SiN membranes. By changing the multilayer structure (periodicity, number of bilayers, etc.) the intensity of the reflected and transmitted beams were optimized for selected incident radiation parameters (wavelength, incident angle). The developed optical elements were characterized by means of XUV reflectometry and transmission measurements, atomic force microscopy and optical interferometry. I paid special attention to the spatial homogeneity of the optical response and reflected beam wavefront distortions. I was the principal investigator in this work, I have designed the multilayer coatings and participated in their characterization.

### 3.10. Summary

**Within the research constituting the habilitation achievement I have defined fundamental processes leading to structural modifications in solids under irradiations with intense femtosecond pulses of XUV and X-ray radiation. In my studies I concentrated on reflecting multilayer coatings and bulk silicon - materials important for optics for new generation of radiation sources, short-wavelength FELs.**

I have developed a theoretical model of structural changes in multilayer coating exposed to intense femtosecond XUV pulses. In contrary to the previously applied models, the current one takes into account not only the irradiation induced local changes of the atomic arrangement (melting, solid-solid phase transition) but also atomic movement over larger length scale (in the order of a few-several nanometers) and modifications of the chemical composition of layers material. The model was confirmed by experimental results for two different multilayer system – Mo/Si and MoN/SiN. Furthermore I have studied processes leading to structural modifications in bulk silicon under irradiations with intense femtosecond XUV pulses at high repetition rate (1 MHz). The experimental results were explained on the base of a heat diffusion model including transition dynamics, energy transfer, and accumulation processes. Using FELs, it became possible to significantly extend optical laser and short-wavelength laser plasma studies of structural phase transitions in solids by systematic investigation of transition dynamics, energy transfer, accumulation of heat and damage. Linear absorption in the XUV and X-ray spectral range, not influenced by irradiation conditions and studied materials, and femtosecond pulse duration allowed to separate processes of energy deposition from transport - in from of heat diffusion or electron-phonon coupling – and following structural modifications – e.g. phase transitions or atomic diffusion. This dramatically simplifies modelling of physical processes leading to structural changes of matter.

Presented research is of practical importance. Apart from new experimental opportunities, the use of an intense FEL beam created extreme demands for optics, primarily on the radiation hardness. **The results of my studies help to specify geometrical constraints and structural requirements for optical elements and radiation detectors for new short wavelength FEL sources. In particular, the model I have developed was used for simulations of the radiation hardness of optical coatings for the “water window” spectral range.** Based on it, maximal acceptable radiation intensities (fluences in the range from several to hundreds of mJ/cm<sup>2</sup>) and best materials combinations allowing for transmission of pulses of highest possible fluence (i.e. of high radiation hardness and high reflectivity, like Mo<sub>2</sub>B<sub>5</sub>/B<sub>4</sub>C, CoO/C, V/Sc) were determined.

My contribution to the research described as my habilitation achievement was leading. I was a principal investigator. I have defined scientific cases, chosen applied experimental techniques (including irradiation conditions, in-situ diagnostics and ex-situ structural characterization techniques), supervised and participated in data acquisition and interpretation, proposed theoretical models explaining the obtained

experimental results, developed software for numerical simulations enabling predictions of damage thresholds for other materials and irradiations conditions. Furthermore I have designed the experimental station and some of its components (in-situ radiation diagnostics, sample mounting system, etc.), supervised their technical implementation and developed some of the applied experimental procedures (alignment, irradiation, detector calibration, threshold fluence estimation for multiple-gaussian beam, etc.). **Experimental set-up and methods developed by me were applied in the presented research and in many other studies.**

## Bibliography

- [1] K. Tiedtke *et al.*, New Journal of Physics **11**, 023029 (2009).
- [2] E. Allaria *et al.*, Nat. Photonics **6**, 699 (2012).
- [3] P. Emma *et al.*, Nat. Photonics **4**, 641 (2010).
- [4] M. Yabashi *et al.*, Journal of Physics B: Atomic, Molecular and Optical Physics **46**, 164001 (2013).
- [5] S. Roling, B. Siemer, M. Wöstmann, H. Zacharias, R. Mitzner, A. Singer, K. Tiedtke, and I. A. Vartanyants, Phys. Rev. ST Accel. Beams **14**, 080701 (2011).
- [6] D. Attwood, *Soft x-rays and extreme ultraviolet radiation: principles and applications* (Cambridge university press, 2007).
- [7] E. Spiller, Bellingham, WA (1994).
- [8] V. Bakshi, *EUV sources for lithography* (SPIE press, 2006), Vol. 149.
- [9] E. Louis *et al.*, in *Emerging Lithographic Technologies IX, Pts 1 and 2*, edited by R. S. Mackay(2005), pp. 1170.
- [10] H. N. Chapman *et al.*, Nature **448**, 676 (2007).
- [11] B. Nagler *et al.*, Nat. Phys. **5**, 693 (2009).
- [12] M. J. R. Sobierajski, D. Klinger, and J. Krzywinski, “R., J.B. Pelka, H. Chapman, S. P. Hau-Riege, R. London, L. Juha, J. Chalupsky, J. Cihelka, K. Tiedtke, S. Toleikis, H. Wabnitz, U. Jastrow, K. Sokolowski-Tinten, N. Stojanovic, HASYLAB Annual Report 2006, 395 (2006).
- [13] S. P. Hau-Riege *et al.*, Phys. Rev. Lett. **98**, 145502 (2007).
- [14] S. P. Hau-Riege, R. A. London, H. N. Chapman, and M. Bergh, Physical Review E **76**, 046403 (2007).
- [15] E. Louis, H. J. Voorma, N. B. Koster, F. Bijkerk, Y. Y. Platonov, S. Y. Zuev, S. S. Andreev, E. A. Shamov, and N. N. Salashchenko, Microelectron. Eng. **27**, 235 (1995).
- [16] E. Louis *et al.*, Microelectron. Eng. **23**, 215 (1994).
- [17] H. J. Voorma, E. Louis, F. Bijkerk, and S. Abdali, J. Appl. Phys. **82**, 1876 (1997).
- [18] E. Louis *et al.*, in *International Symposium on Optical Science and Technology* (International Society for Optics and Photonics, 2000), pp. 60.
- [19] I. Nedelcu, R. W. E. v. de Kruijs, A. E. Yakshin, and F. Bijkerk, J. Appl. Phys. **103**, 083549 (2008).
- [20] V. V. Kondratenko *et al.*, Applied Optics **32**, 1811 (1993).
- [21] J. M. Liang and L. J. Chen, J. Appl. Phys. **79**, 4072 (1996).
- [22] I. Nedelcu, R. W. E. van de Kruijs, A. E. Yakshin, and F. Bijkerk, Phys. Rev. B **76**, 245404 (2007).
- [23] P. Jonnard, I. Jarrige, R. Benbalagh, H. Maury, J. M. Andre, Z. Dankhazi, and G. Rolland, Surface Science **589**, 164 (2005).
- [24] J. R. Chelikowsky, N. Troullier, and N. Binggeli, Phys. Rev. B **49**, 114 (1994).
- [25] F. De Boer, R. Boom, W. Mattens, and A. Miedema, Transition Metal Alloys, North-Holland, Amsterdam (1988).
- [26] B. L. Henke, E. M. Gullikson, and J. C. Davis, Atomic Data and Nuclear Data Tables **54**, 181 (1993).
- [27] K. H. Tsang, H. W. Kui, and K. P. Chik, J. Appl. Phys. **74**, 4932 (1993).
- [28] D. L. Lide, *CRC Handbook of Chemistry and Physics, 90th Edition* 2009-2010).
- [29] M. Grimaldi, P. Baeri, M. Malvezzi, and C. Sirtori, International journal of thermophysics **13**, 141 (1992).
- [30] S. Roorda, S. Doorn, W. C. Sinke, P. Scholte, and E. Vanloenen, Phys. Rev. Lett. **62**, 1880 (1989).
- [31] E. P. Donovan, F. Spaepen, D. Turnbull, J. M. Poate, and D. C. Jacobson, Applied Physics Letters **42**, 698 (1983).
- [32] The heat conductivity of thin film amorphous silicon was measured independently by different groups to be equal to 1.5W/m-K and almost independent of temperature, while the conductivity in liquid Si is significantly higher: 62 W/m-K. Assuming similar behavior of the heat conductivity of thin film Mo compared to other thin metallic films I used in my calculations  $25 \pm 15$  W/m-K as the heat conductivity of the Mo layers.
- [33] S. Volz, X. Feng, C. Fuentes, P. Guerin, and M. Jaouen, International Journal of Thermophysics **23**, 1645 (2002).
- [34] S. Moon, M. Hatano, M. H. Lee, and C. P. Grigoropoulos, International Journal of Heat and Mass Transfer **45**, 2439, Pii s0017-9310(01)00347-7 (2002).
- [35] P. B. Allen and J. L. Feldman, Phys. Rev. Lett. **62**, 645 (1989).
- [36] H. Kobatake, H. Fukuyama, I. Minato, T. Tsukada, and S. Awaji, Applied Physics Letters **90**, 094102 (2007).
- [37] T. Yamane, Y. Mori, S. Katayama, and M. Todoki, J. Appl. Phys. **82**, 1153 (1997).

- [38] B. Feng, Z. Li, and X. Zhang, *Thin Solid Films* **517**, 2803 (2009).
- [39] H. Nakajima, M. Ikebe, Y. Muto, S. Yamaguchi, and H. Fujimori, *MRS Int'l. on Adv. Mats.* **10**, 405 (1989).
- [40] E. Louis, H. J. Voorma, N. B. Koster, F. Bijkerk, Y. Y. Platonov, S. Y. Zuev, S. S. Andreev, E. A. Shamov, and N. N. Salashchenko, *Microelectron. Eng.* **27**, 235 (1995).
- [41] E. Louis *et al.*, edited by A. D. Elizabeth (SPIE, 2000), pp. 406.
- [42] R. Kärcher, L. Ley, and R. L. Johnson, *Phys. Rev. B* **30**, 1896, 1984 (1984).
- [43] I. Kusunoki, T. Takaoka, Y. Igari, and K. Ohtsuka, *J. Chem. Phys.* **101**, 8238, 1994 (1994).
- [44] E. P. Donovan, G. K. Hubler, M. S. Mudholkar, and L. T. Thompson, *Surf. Coat. Tech.* **66**, 499, 1994 (1994).
- [45] D. L. Windt, *Comput. Phys.* **12**, 360 (1998).
- [46] H. Jehn and P. Ettmayer, *J. of the Less Common Met.* **58**, 85, 1978 (1978).
- [47] K. Frisk, *Calphad* **15**, 79 (1991).
- [48] B. Ziaja, R. A. London, and J. Hajdu, *J. Appl. Phys.* **99**, 033514 (2006).
- [49] A. E. Morris, H. A. Fine, and G. Geiger, *Handbook on Material and Energy Balance Calculations in Material Processing, Includes CD-ROM* (John Wiley & Sons, 2011).
- [50] F. Eriksson, N. Ghafoor, F. Schaefer, E. M. Gullikson, S. Aouadi, S. Rohde, L. Hultman, and J. Birch, *Applied Optics* **47**, 4196 (2008).
- [51] C. Montcalm, P. A. Kearney, J. M. Slaughter, B. T. Sullivan, M. Chaker, H. Pepin, and C. M. Falco, *Applied Optics* **35**, 5134 (1996).
- [52] F. Eriksson, Linköping studies in science and technology-dissertations- (2004).
- [53] K. Honkavaara, B. Faatz, J. Feldhaus, S. Schreiber, R. Treusch, and M. Vogt, (2015).
- [54] N. Stojanovic *et al.*, *Appl. Phys. Lett.* **89**, 241909 (2006).
- [55] D. W. Bäuerle, *Laser processing and chemistry* (Springer Science & Business Media, 2013).
- [56] R. Sobierajski *et al.*, in *Damage to VUV, EUV, and X-Ray Optics II*, edited by S. B. Libor Juha, Ryszard Sobierajski (SPIE, Prague, 2009).
- [57] T. Koyama *et al.*, *Journal of Physics: Conference Series* **463**, 012043 (2013).
- [58] T. Koyama *et al.*, *Opt. Express* **21**, 15382 (2013).
- [59] N. Medvedev, Z. Li, and B. Ziaja, *Phys. Rev. B* **91**, 054113 (2015).
- [60] H. Hu and S. A. Argyropoulos, *Modelling and Simulation in Materials Science and Engineering* **4**, 371 (1996).
- [61] Material's thermodynamical parameterers taken from NIST Chemistry WebBook, <http://webbook.nist.gov/chemistry/>.
- [62] H. Shanks, P. Maycock, P. Sidles, and G. Danielson, *Physical Review* **130**, 1743 (1963).
- [63] A. Rämer, O. Osmani, and B. Rethfeld, *J. Appl. Phys.* **116**, 053508 (2014).

**Spis treści**

1. Personal data.....	1
2. Scientific achievement – major results.....	1
3. Detailed description of the achievement.....	3
3.1. The scope of the work .....	3
3.2. Introduction.....	3
3.3. Experimental set-up and procedures at FLASH [H4].....	4
3.4. Radiation hardness of Mo/Si multilayer coatings for FEL optics [H1] .....	12
3.5. Radiation hardness of MoN/SiN multilayer coatings for FEL optics [H2].....	16
3.6. Modeling single shot damage thresholds of multilayer optics for high-intensity short-wavelength radiation sources [H5] .....	22
3.7. The role of heat accumulation on the multi-shot damage of silicon irradiated with femtosecond XUV pulses at a 1 MHz repetition rate. ....	25
3.8. Other work related to the scientific achievement. ....	29
3.9. Other activities unrelated to the scientific achievement .....	32
3.10. Summary .....	33
Bibliography.....	35

